Monthly Notices
of the
ROYAL ASTRONOMICAL SOCIETY

MNRAS **465,** 858–884 (2017)
Advance Access publication 2016 October 13

doi:10.1093/mnras/stw2621

Chandra measurements of a complete sample of X-ray luminous galaxy clusters: the luminosity–mass relation

P. A. Giles,[1⋆] B. J. Maughan,[1] H. Dahle,[2] M. Bonamente,[3,4] D. Landry,[3] C. Jones,[5] M. Joy,[4] S. S. Murray[5] and N. van der Pyl[1]

[1]*HH Wills Physics Laboratory, Tyndall Avenue, Bristol BS8 1TL, UK*
[2]*Institute of Theoretical Astrophysics, University of Oslo, PO Box 1029, Blindern, N-0315 Oslo, Norway*
[3]*Physics Department, University of Alabama in Huntsville, Huntsville, AL 35899, USA*
[4]*NASA National Space Science and Technology Center, Huntsville, AL 35812, USA*
[5]*Harvard–Smithsonian Center for Astrophysics, 60 Garden Street, Cambridge, MA 02138, USA*

Accepted 2016 October 9. Received 2016 October 3; in original form 2015 October 14

ABSTRACT

We present the results of work involving a statistically complete sample of 34 galaxy clusters, in the redshift range $0.15 \leq z \leq 0.3$ observed with *Chandra*. We investigate the luminosity–mass (*LM*) relation for the cluster sample, with the masses obtained via a full hydrostatic mass analysis. We utilize a method to fully account for selection biases when modelling the *LM* relation, and find that the *LM* relation is significantly different from the relation modelled when not account for selection effects. We find that the luminosity of our clusters is 2.2 ± 0.4 times higher (when accounting for selection effects) than the average for a given mass and its mass is 30 per cent lower than the population average for a given luminosity. Equivalently, using the *LM* relation measured from this sample without correcting for selection biases would lead to the underestimation by 40 per cent of the average mass of a cluster with a given luminosity. Comparing the hydrostatic masses to mass estimates determined from the Y_X parameter, we find that they are entirely consistent, irrespective of the dynamical state of the cluster.

Key words: galaxies: clusters: general – X-rays: galaxies: clusters.

1 INTRODUCTION

Clusters of galaxies are the largest gravitationally collapsed structures in the Universe. Studying properties such as the number density of clusters and details of their growth from the highest density perturbations in the early Universe offers insight into the underlying cosmology (e.g. Mantz et al. 2008; Vikhlinin et al. 2009b; Planck Collaboration XXIV 2016b). The study of galaxy clusters has been transformed with the launch of powerful X-ray telescopes such as *Chandra* and *XMM*, which have allowed the study of the X-ray emitting intracluster medium (ICM) with unprecedented detail and accuracy. Cluster properties have been used widely in the determination of cosmological parameters. Cosmological studies utilizing clusters include investigating the cluster temperature function (e.g. Henry & Arnaud 1991; Henry 1997; Eke et al. 1998; Ikebe et al. 2002), scaling relations such as the luminosity–mass (*LM*; e.g. Reiprich & Böhringer 2002; Stanek et al. 2006) and the temperature–mass (*TM*; e.g. Vikhlinin et al. 2006) relations, using the gas mass fraction, $f_{\rm gas}$ (Allen et al. 2008; Mantz et al. 2014), the cluster mass function (e.g. Vikhlinin et al. 2009b) and the cluster luminosity function (e.g. Böhringer, Chon & Collins 2014; Pacaud et al. 2016), to place constraints on various cosmological parameters. Since one of the most important ingredients of these cosmological studies is the cluster mass, large efforts have been undertaken to accurately determine this quantity. One such method involves the construction of radial temperature and gas density profiles of the ICM, and under the assumption of hydrostatic equilibrium, the cluster mass can be determined.

Observations using X-rays have become a well-established method of estimating cluster masses. However, constructing temperature profiles for individual clusters for use in a hydrostatic mass analysis generally requires long telescope exposure times, and not is not feasible for large samples of clusters. Therefore, deriving well-calibrated scaling relations between simple cluster observables and mass is of crucial importance for using clusters as cosmological probes (e.g. Mantz et al. 2010b). The X-ray luminosity (L) is one of the easiest cluster properties to obtain, and has had a rich history in its scaling with mass (M). Under the assumption of self-similarity (Kaiser 1986), the *LM* relation (throughout this work we use the notation *LM* when generally discussing the luminosity–mass relation) is expected to follow a relationship of $L \propto M^{4/3}$. However, observational studies of the *LM* relation have found a slope steeper than the self-similar expectation (e.g. Rykoff et al. 2008; Pratt et al. 2009; Connor et al. 2014). The most widely accepted theory for the steep slope of the *LM* relation is due to heating from sources such

⋆ E-mail: P.Giles@bristol.ac.uk

as supernovae and active galactic nuclei feedback (e.g. Short et al. 2010; McCarthy et al. 2011; Le Brun et al. 2014). This causes gas to be expelled from the inner region, hence suppressing the luminosity. This effect should be larger in lower mass systems due to the shallower potential well, which therefore causes the observed steepening of the *LM* relation.

A complication of measuring the *LM* relation is that the cluster samples used are traditionally X-ray selected, with X-ray flux-limited samples suffering from two forms of selection bias, Malmquist bias, where higher luminosity clusters are detectable out to higher redshifts and so occupy a larger survey volume, and Eddington bias, where in the presence of intrinsic or statistical scatter in luminosity for a given mass, objects above a flux limit will have above-average luminosities for their mass. Due to the steep slope of the cluster mass function, the Eddington bias is amplified, resulting in a net movement of lower mass objects into a flux-limited sample. The consequence of biases on the observed *LM* relation is to bias the normalization high and the slope low (see Allen, Evrard & Mantz 2011). Therefore, taking these biases into account is paramount when modelling cluster scaling relations, in order to uncover the true nature of any non-gravitational heating which drives departures from self-similar behaviour with mass or redshift. Although scaling relation studies have had a rich history, at the present time only a small number of published relations attempt to account for selection biases (e.g. Stanek et al. 2006; Pacaud et al. 2007; Pratt et al. 2009; Vikhlinin et al. 2009a; Andreon 2012; Bharadwaj et al. 2015; Lovisari, Reiprich & Schellenberger 2015; Sereno & Ettori 2015), while Mantz et al. (2010a, hereafter M10a) provide the most robust handling of selection effects to date.

Deriving cluster masses through X-ray observations with the assumption that the ICM is in hydrostatic equilibrium is not always valid, as some clusters have complex temperature structures due to processes such as merger events. Relaxed systems have traditionally been used for the determination of X-ray masses, as departures from hydrostatic equilibrium are minimized for these systems (e.g. Nagai, Kravtsov & Vikhlinin 2007). Therefore, methods have been developed to infer the cluster dynamical state (e.g. Poole et al. 2006; Mantz et al. 2015). Furthermore, clusters that appear to host a cool core (CC) are frequently used for mass derivations as they are believed to be dynamically relaxed. However, the presence of a CC alone cannot be used to accurately determine the dynamical state.

Many methods are used to infer the presence of a CC (see Hudson et al. 2010, for a comprehensive study), including measuring the central temperature drop (e.g. O'Hara et al. 2006), the central cooling time (CCT; e.g. Bauer et al. 2005; Santos et al. 2010; Mittal et al. 2011), the core entropy (e.g. Comis et al. 2011) and the cuspiness of the gas density profile (Vikhlinin et al. 2007). Frequently, cheaply obtainable cluster properties such as luminosity and temperature are used as a mass proxy, using well-calibrated scaling relations, to calculate the masses of large cluster samples. This first requires constructing scaling relations for dynamically relaxed clusters, and then inferring the cluster masses from these relations. It has been found however that using CC clusters sometimes results in larger scatter of the *LM* scaling relation compared to non-cool core (NCC) clusters (e.g. O'Hara et al. 2006). Maughan et al. (2012) found that by defining a cluster subsample using clusters appearing both dynamically relaxed and hosting a CC, the luminosity–temperature (*LT*) relation appears self-similar, compared to unrelaxed and NCC clusters. While this method may be the preferred choice for defining subsamples of clusters for mass derivations, this limits the cluster sample size used for mass calculations; thus, the derived scaling relation may not be representative of the whole cluster population.

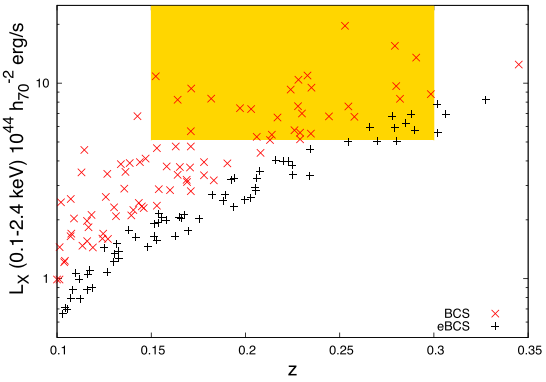

Figure 1. Plot of the luminosity–redshift distribution of the BCS and eBCS clusters. The yellow shaded region highlights the region enclosed by the luminosity and redshift cuts imposed to define our cluster sample (see Section 2).

This paper aims to measure the masses for a complete sample of 34 clusters to measure the X-ray *LM* scaling relation, utilizing hydrostatic mass estimates and fully accounting for selection effects. The outline of the paper is as follows. In Section 2, we discuss the sample selection and data analysis. Section 3 details the cluster analysis and determines the dynamical state of individual clusters. Notes on individual clusters are given in Section 4. Our results are presented in Section 5. The discussion and conclusions are presented in Sections 6 and 7, respectively. Throughout this paper, we assume a *Wilkinson Microwave Anisotropy Probe* 9 (*WMAP*9) cosmology of $H_0 = 69.7$ km s^{-1} Mpc^{-1}, $\Omega_M = 0.282$, $\Omega_\Lambda = 0.718$ and $\sigma_8 = 0.817$ (Hinshaw et al. 2013).

2 SAMPLE AND DATA PREPARATION

The sample of clusters used in our analysis was defined by the conditions given in Dahle (2006). The sample of clusters represents a complete sample of X-ray luminous clusters taken from the RASS-based, X-ray flux-limited *ROSAT* Brightest Cluster Sample (BCS) of Ebeling et al. (1998) and its low-flux extension (eBCS; Ebeling et al. 2000). Dahle (2006) imposed a lower cutoff in X-ray luminosity of $L_{X,0.1-2.4\,keV} = 6 \times 10^{44}$ erg s^{-1} (the limit based upon a cosmology assuming $\Omega_M = 0.3$, $\Omega_\Lambda = 0.7$ and $h = 0.7$), corresponding to a sample of 36 clusters within the redshift range $0.15 \leq z \leq 0.30$. Fig. 1 plots the luminosity–redshift distribution of the BCS and eBCS, with the yellow shaded region highlighting the region enclosed by the luminosity and redshift cuts defining our sample selection. Note that two of the clusters were dropped from the cluster sample, as detailed below, leading to a final sample of 34 clusters.

The cluster A689 satisfies these selection criteria, but was noted in the original detection as having a large portion of its flux coming from embedded point sources, and was therefore excluded from the cluster sample. The source of the embedded point source was found to be a central BL-Lac object (Giles et al. 2012), with the re-analysis determining a cluster X-ray luminosity ∼10 times lower than quoted in the BCS, well below the sample cutoff X-ray luminosity. Furthermore, we found that the redshift given for the cluster Zw5768 in Ebeling et al. (1998) was incorrect. With the correct (lower) redshift, the cluster drops below the luminosity limit of our sample and was rejected (see Section 4). For the X-ray analysis, we obtained *Chandra* observations to complete the sample and

Table 1. Cluster sample and *Chandra* observations. Column 1: cluster name; column 2: RA; column 3: DEC; column 4: cluster redshift; column 5: luminosity from Ebeling et al. (1998, 2000), converted to a ΛCDM cosmology; column 6: *Chandra* ObsID; column 7: *Chandra* aim point; column 8: cleaned exposure time.

Cluster	RA (J2000.0)	Dec. (J2000.0)	z	$L_{X,BCS,0.1-2.4\,keV}$ (10^{44} erg s^{-1})	*Chandra* observations ObsID	Aim point	Exposure (ks)
A2204	16 32 47.04	+05 34 31.26	0.152	12.51 ± 1.34	6104, 7940	I	86.8
RXJ1720.1+2638	17 20 10.08	+26 37 29.28	0.164	9.58 ± 1.08	1453, 3224, 4361	I	45.2
A586	07 32 20.40	+31 37 56.28	0.171	6.64 ± 1.30	11723	I	9.91
A1914	14 23 00.96	+37 49 33.96	0.171	10.99 ± 1.11	3593	I	18.9
A665	08 30 57.36	+65 50 33.36	0.182	9.84 ± 1.54	12286, 13201	I	26.4
A115	00 55 50.69	+26 24 37.80	0.197	8.90 ± 2.13	13458, 13459, 15578	I	282
A520	04 54 10.00	+02 55 18.16	0.203	8.85 ± 1.99	9424, 9425, 9426, 9430	I	447
A963	10 17 30.36	+39 02 53.88	0.206	6.39 ± 1.18	903	S	35.8
A1423	11 57 19.28	+33 36 41.08	0.213	6.19 ± 1.34	538, 11724	I	35.6
A773	09 17 53.04	+51 43 39.36	0.217	8.99 ± 1.35	533, 3588, 5006	I	40.1
A1763	13 35 18.24	+40 59 59.28	0.223	9.32 ± 1.33	3591	I	19.6
A2261	17 22 27.12	+32 07 56.64	0.224	11.32 ± 1.55	5007	I	24.1
A1682	13 06 50.40	+43 33 26.28	0.226	7.02 ± 1.37	11725	I	19.9
A2111	15 39 41.52	+34 25 50.16	0.229	6.83 ± 1.66	544, 11726	I	31.2
Zw5247	12 34 18.96	+09 46 12.86	0.229	6.32 ± 1.58	11727	I	19.7
A267	01 52 42.14	+01 00 41.30	0.230	8.57 ± 1.80	1448	I	7.29
A2219	16 40 20.40	+46 42 29.52	0.230	12.74 ± 1.37	14355, 14356, 14431	I	118
A2390	21 53 36.72	+17 41 44.52	0.233	13.43 ± 3.14	4193	S	22.0
Zw2089	09 00 36.96	+20 53 40.20	0.235	6.79 ± 1.76	10463	S	40.1
RXJ2129.6+0005	+21 29 40.10	00 05 20.91	0.235	11.67 ± 2.92	552, 9370	I	39.6
A1835	14 01 10.92	+02 52 42.47	0.253	24.49 ± 3.35	6880, 6881, 7370	I	193.2
A68	00 37 60.09	+09 09 33.05	0.255	9.48 ± 2.61	3250	I	9.99
MS1455.0+2232	14 57 15.12	+22 20 35.52	0.258	8.41 ± 2.10	4192	I	91.37
A2631	23 37 38.16	+00 16 90.11	0.278	8.57 ± 1.80	3248, 11728	I	25.9
A1758N	13 32 38.88	+50 33 38.88	0.279	7.51 ± 1.61	13997, 15538, 15540	I	147
A1576	12 36 58.32	+63 11 19.68	0.279	7.20 ± 1.80	7938, 15127	I	43.1
A697	08 42 57.60	+36 21 55.80	0.282	10.57 ± 3.28	4217	I	17.4
RXJ0439.0+0715	04 39 00.67	+07 16 30.76	0.285	8.37 ± 2.55	1449, 3583	I	20.5
RXJ0437.1+0043	04 37 90.46	+00 43 54.15	0.285	7.96 ± 2.34	7900, 11729	I	42.5
A611	08 00 56.64	+36 03 23.40	0.288	8.86 ± 2.53	3194	S	15.4
Zw7215	15 01 23.04	+42 20 54.96	0.290	7.34 ± 1.91	7899	I	13.0
Zw3146	10 23 39.60	+04 11 12.88	0.291	17.27 ± 2.94	909, 9371	I	78.7
A781	09 20 26.16	+30 30 20.52	0.298	11.29 ± 2.82	534, 15128	I	45.0
A2552	23 11 33.12	+03 38 60.93	0.302	10.08 ± 2.88	11730	I	22.6

downloaded archived observations of the remaining clusters from the *Chandra* data archive.

All 34 galaxy clusters in this sample were analysed with the CIAO[1] 4.6 software package and CALDB[2] version 4.5.9 (Fruscione et al. 2006). We applied standard processing techniques to the level 1 photon lists to generate a level 2 photon list. We inspected background light curves of the observations following the recommendations of Markevitch et al. (2003), to search for possible background fluctuations. The light curves were cleaned by 3σ clipping and periods with count rates >20 per cent deviation from the mean rate were rejected. The final cleaned exposure times are listed in Table 1.

In order to take into account the background of each observation, appropriate blank-sky backgrounds were obtained (which are processed identically to the cluster observations) and reprojected on to the sky to match the cluster observation. For background data sets taken after 2001 December 1, the background observations were telemered in VFAINT mode. Therefore, the additional VFAINT cleaning procedure was applied to the source and background data sets.[3]

We followed a method outlined in Vikhlinin et al. (2005) in order to improve the accuracy of the background by applying small adjustments to the baseline model. We first corrected for the rate of charged particle events, which has a secular and short-term variation by as much as 30 per cent. We renormalize the background in the 9.5–12 keV band, where the *Chandra* effective area is nearly zero and the observed flux is due entirely to the particle background events. The renormalization factor was derived by taking the ratio of the observed count rate in the source and background observations, respectively. In addition to the particle background, the blank-sky and source observations contain differing contributions from the soft X-ray background, containing a mixture of the Galactic and geocoronal backgrounds, significant at energies ≤1 keV. To take into account any difference in this background component between the blank-sky and source observations, spectra were extracted in regions of the field of view free from cluster emission. The blank-sky spectrum was then subtracted from that of the local background, and the residuals modelled in the 0.4–1 keV band using an APEC thermal plasma model (Smith et al. 2001), with the abundance set to solar and assuming zero redshift. This component is usually adequately described with a temperature 0.18 keV; however, in the cases when this produced a poor fit to the residuals, the temperature was allowed to be free and then fixed at the value which produced the best fit (see Section 4 for the cases when this was applied).

[1] See http://cxc.harvard.edu/ciao/
[2] See http://cxc.harvard.edu/caldb/
[3] See http://cxc.harvard.edu/ciao/why/aciscleanvf.html

This component was then included in the spectral modelling of the cluster (see Section 3.1).

3 DATA ANALYSIS

In this section, we detail the data analysis performed on our sample of clusters. The analysis follows closely the analysis presented in Maughan et al. (2012), which was closely based in turn on Vikhlinin et al. (2005). Any deviations from this standard analysis are described in the following sections.

3.1 Cluster spectral properties

Cluster spectra were extracted and fits performed in the 0.6–9.0 keV band with an absorbed APEC plasma model (using ATOMDB version 2.0.1, and relative abundances fixed to the solar ratios of Anders & Grevesse 1989). The absorbing column was fixed at the Galactic value (Kalberla et al. 2005) and the abundance allowed to vary. The fits were performed in XSPEC (Arnaud 1996) using the *C*-statistic (the use of the *C*-statistic is discussed further in Section 6.2), with the spectra grouped to contain at least one count per bin. When determining the uncertainties on the temperature, the uncertainty due to the modelling of the soft background component was estimated as the variation in the temperature of the cluster component when the normalization of the soft background component (see Section 2) was set to $\pm 1\sigma$ of the fitted value. This error term was then added in quadrature to the original statistical error on the temperature to produce the final temperature error bar. Since many of the clusters in the sample contained multiple *Chandra* observations, the individual observations were analysed separately as outlined below. The data were then combined for certain stages of the analysis. Source and background spectra were extracted as below for individual observations and fit simultaneously with the temperature, abundance and normalizations of the APEC components tied together and the redshift and absorbing column fixed.

The cluster properties were derived within r_{500} (including the cluster core), the radius at which the density of the cluster becomes 500 times the critical density of the Universe at the cluster redshift. Estimates of the cluster r_{500} were estimated from the cluster mass, based on a hydrostatic mass ($M_{\rm H}$) analysis (see Sections 3.3 and 3.4). We denote $L_{\rm CXO}$ and $L_{\rm bol}$ as the unabsorbed 0.1–2.4 keV (rest-frame) and bolometric luminosities, respectively.

3.2 Gas density modelling

We make use of the observed projected emissivity profile to accurately measure and model the gas density profile. We converted each annular bin in the background-subtracted, exposure-corrected surface brightness profile (measured in the 0.7–2.0 keV band, constructed such that each bin contained at least 50 cluster counts) into an integrated emission measure for each annulus. The conversion factor was determined by extracting an Auxiliary Response File and Redistribution Matrix File in each annular bin and using these, we simulate a spectrum assuming an absorbed APEC model. The absorption was set at the Galactic value (Kalberla et al. 2005) and the metal abundance set to 0.3 solar. As the data in each annular bin were not sufficient to measure a temperature, the temperature of the model in each bin was obtained by utilizing the average temperature profile found by Vikhlinin et al. (2006), depending on the radius of the bin, the determined r_{500} and the global temperature for each cluster. The normalization of the spectral model was set to 1 and re-arranged to determine the emission integral for each bin given the derived count rate.

The gas density profile was then fitted with a modified version of the standard 1D β-model proposed by Vikhlinin et al. (2006, hereafter V06),

$$n_{\rm p} n_{\rm e} = n_0^2 \frac{(r/r_{\rm c})^{-\alpha}}{(1+r^2/r_{\rm c}^2)^{3\beta-\alpha/2}} \frac{1}{(1+r^{\gamma}/r_{\rm s}^{\gamma})^{\epsilon/\gamma}}. \quad (1)$$

We employ the same constraints as employed by V06, i.e. γ is fixed at 3 and $\epsilon < 5$ to exclude non-physical sharp density breaks. We simplify the model slightly by excluding the second β-model component outlined in V06, so that the model could be used to fit to higher and lower quality data in our sample.

This model was then projected along the line of sight and fitted to the observed projected emission measure profile. The parameters in equation (1) are strongly correlated and therefore the individual parameters degenerate. For this reason, the uncertainty on the derived density profile was estimated by generating synthetic emissivity profiles, where each data point in the original profile was replaced by a value sampled from a Gaussian centred on the value of the best-fitting model with a standard deviation equal to the measurement error for that point. 1000 such synthetic data sets were generated and fitted as before to give 1000 output density profiles. These were used in all subsequent analyses to propagate the uncertainties on the gas density profile. The individual parameters for each cluster can be found in Appendix A (Table A1).

3.3 Temperature profile modelling

To determine the total hydrostatic mass of a cluster, we use the method outlined in V06. This requires the use of a projected temperature profile. The temperature profile is constructed such that it describes the temperature decline in the central regions of most clusters, and a description for the profile in the outer regions of a cluster. The profile in the central regions of a cluster can be described as

$$T_{\rm cool}(r) = \frac{(x + T_{\rm min}/T_0)}{(x+1)}, \quad x = \left(\frac{r}{r_{\rm cool}}\right)^{a_{\rm cool}}. \quad (2)$$

Outside the cooling region, the temperature profile can be represented by

$$T(r) = \frac{(r/r_{\rm t})^{-a}}{[1+(r/r_{\rm t})^b]^{c/b}}. \quad (3)$$

The final three-dimensional temperature profile is then given by

$$T_{\rm 3D}(r) = T_0 T_{\rm cool}(r) T(r). \quad (4)$$

For our clusters, the temperature profiles were constructed by creating concentric annuli centred on the cluster such that each annulus was a specific fraction of the determined r_{500}. To determine the r_{500} for the temperature profile binning, we constructed temperature profiles with each bin containing a minimum of 700 cluster counts. A mass analysis was performed (following Section 3.4) using these initial temperature profiles, and an initial r_{500} calculated. For clusters with greater than 10 temperature bins in this initial temperature profile, the profiles were rescaled to simply contain 10 bins, with the bins rescaled to specific fractions of the initial r_{500}. The fractions of r_{500} were calculated based on having a minimum signal-to-noise (S/N) of 20, and were calculated based on the lowest S/N cluster with greater than 10 temperature bins. For clusters with fewer than 10 temperature bins in the initial profile, the initial number of bins were simply rescaled to fractions of the initial r_{500}. With temperature profiles constructed such that the bins are defined

in fractions of r_{500}, a second mass analysis is performed to determine the final r_{500} and hydrostatic mass. This method ensures that the mass estimates for the clusters are derived in a consistent way. Furthermore, the errors on the temperature for each radial bin are converted to account for the fact that the likelihood curve for a measured temperature is approximately Gaussian in log space. We use the method of Andreon (2012) to convert the generally asymmetric errors reported by XSPEC into a lognormal likelihood.

The temperature profile model (equation 4) was fitted to the data by projecting it along the line of sight (using a method outlined in Vikhlinin 2006) and computing the χ^2 in the log of the temperature (Table A2 lists the individual fit parameters for our clusters, and the figures of the temperature profiles with the corresponding fit are presented). This model has great functional freedom with nine free parameters and can describe many smooth temperature distributions. To take into account the uncertainties on the temperature profile, we follow the same Monte Carlo method as that employed in Section 3.2, generating and refitting synthetic temperature profiles based on the initial model. For the cases when the number of bins in the temperature profile is less than the nine free parameters, one or more of the parameters are frozen at values given by the average temperature profile given in V06. The constraints imposed when fitting to a temperature profile with low-temperature bins are as follows.

(1) No cool core: $x = 1$ and $T_0 = T_{\rm min}$ in equation (2).
(2) $b = c$ and $a = 0$.
(3) No cool core, $b =$ c and $a = 0$.

The constraints (1), (2) and (3) were employed when a cluster's temperature profile had seven to nine, six and five bins, respectively.

3.4 X-ray hydrostatic mass derivation

To derive the total hydrostatic mass of the cluster, within a radius r, we use the three-dimensional models of the temperature profile, $T(r)$, and gas density profile, obtained by a fit to the emission measure profile converted to a gas density, $\rho_{\rm g}(r)$, and the hydrostatic equilibrium equation (Sarazin 1988),

$$M(r) = -\frac{kT(r)r}{\mu m_{\rm p} G}\left(\frac{{\rm d}\log T(r)}{{\rm d}\log r} + \frac{{\rm d}\log \rho_{\rm g}(r)}{{\rm d}\log r}\right), \quad (5)$$

where k is the Boltzmann constant and μ corresponds to the mean molecular weight in units of $m_{\rm p}$ (where $\mu = 0.5954$), where $m_{\rm p}$ is the mass of a proton. The gas density profile and temperature profiles are constructed using the method outlined in Sections 3.2 and 3.3, respectively.

3.5 Determining the dynamical state of a cluster

Here we wish to determine which clusters in our sample both appear dynamically relaxed and host a CC (RCC).

We first determine which clusters in our sample are dynamically relaxed. The dynamical state of the cluster was measured using the centroid shift ($\langle w \rangle$), following the method of Poole et al. (2006). The centroid shift was defined as the standard deviation of the distance between the X-ray peak and the centroid. The centroid was measured within a series of circular apertures centred on the X-ray peak, with the apertures decreasing in size from r_{500} to $0.05\,r_{500}$, in steps of $0.05\,r_{500}$. The errors on $\langle w \rangle$ were derived by producing 100 Monte Carlo randomizations of the input source and background images with pixels randomized under a Poisson distribution centred on the observed counts in each pixel. These were then analysed in the same way as the real images to give a distribution of $\langle w \rangle$, from which we used the standard deviation as an estimate of the error on $\langle w \rangle$. The values of $\langle w \rangle$ are given in Table 2. We make a cut at $\langle w \rangle = 0.009$, above which clusters are classed as dynamically unrelaxed, and below which clusters are classed as dynamically relaxed. This value was chosen when visually inspecting images of each cluster ranked in order of $\langle w \rangle$ and seeing a clear change in the structure of the clusters above this value. This value is close to the value determined by Weißmann et al. (2013), who found that $\langle w \rangle = 0.01$ was the value of choice to split between relaxed and unrelaxed clusters for a sample of 121 simulated clusters. A value of $\langle w \rangle = 0.01$ was also used in Pratt et al. (2009) to split between relaxed and unrelaxed clusters for the REXCESS sample of clusters.

Table 2. Dynamical properties of the cluster sample. Column 1: cluster name; column 2: cuspiness measured as the logarithmic slope of the gas density profile at $0.04r_{500}$; column 3: cooling time measured within $0.048r_{500}$; column 4: centroid shift.

Cluster	Cuspiness	$t_{\rm cool}$ (Gyr)	$\langle w \rangle$ $10^{-3}r_{500}$
A2204[a]	$1.25^{+0.01}_{-0.01}$	$2.03^{+0.01}_{-0.01}$	0.55 ± 0.07
RXJ1720.1+2638[a]	$1.08^{+0.01}_{-0.01}$	$2.36^{+0.03}_{-0.03}$	1.01 ± 0.21
A586	$0.38^{+0.07}_{-0.07}$	$4.86^{+0.44}_{-0.37}$	9.16 ± 4.45
A1914	$0.26^{+0.02}_{-0.01}$	$7.20^{+0.41}_{-0.43}$	13.7 ± 1.28
A665	$0.55^{+0.02}_{-0.01}$	$8.33^{+0.22}_{-0.23}$	40.9 ± 1.33
A115	$1.04^{+0.01}_{-0.01}$	$2.57^{+0.03}_{-0.02}$	86.9 ± 0.33
A520	$0.04^{+0.02}_{-0.01}$	$22.6^{+0.90}_{-1.00}$	53.6 ± 3.04
A963	$0.63^{+0.02}_{-0.02}$	$3.74^{+0.11}_{-0.12}$	2.42 ± 1.36
A1423[a]	$0.80^{+0.03}_{-0.03}$	$3.34^{+0.15}_{-0.14}$	6.11 ± 1.61
A773	$0.24^{+0.06}_{-0.03}$	$10.0^{+0.82}_{-0.80}$	6.27 ± 2.02
A1763	$0.23^{+0.07}_{-0.03}$	$11.1^{+1.59}_{-2.60}$	5.14 ± 3.87
A2261	$0.65^{+0.03}_{-0.03}$	$3.11^{+0.13}_{-0.13}$	9.27 ± 1.02
A1682	$0.42^{+0.08}_{-0.11}$	$8.07^{+1.83}_{-1.54}$	38.6 ± 3.31
A2111	$0.15^{+0.11}_{-0.05}$	$11.1^{+1.27}_{-1.38}$	30.1 ± 11.3
Zw5247	$0.55^{+0.07}_{-0.12}$	$20.9^{+4.89}_{-3.87}$	59.8 ± 28.3
A267	$0.19^{+0.15}_{-0.04}$	$5.67^{+1.04}_{-0.88}$	26.2 ± 14.1
A2219	$0.30^{+0.03}_{-0.04}$	$10.2^{+0.49}_{-0.50}$	14.7 ± 4.81
A2390	$0.99^{+0.01}_{-0.02}$	$5.37^{+0.06}_{-0.07}$	9.81 ± 0.20
Zw2089[a]	$1.10^{+0.02}_{-0.01}$	$1.01^{+0.02}_{-0.02}$	4.87 ± 0.71
RXJ2129.6+0005[a]	$1.01^{+0.01}_{-0.01}$	$1.70^{+0.04}_{-0.04}$	8.37 ± 1.78
A1835[a]	$1.22^{+0.01}_{-0.01}$	$1.19^{+0.01}_{-0.01}$	2.73 ± 0.43
A68	$0.31^{+0.12}_{-0.12}$	$12.0^{+3.37}_{-2.95}$	10.4 ± 2.92
MS1455.0+2232[a]	$1.01^{+0.01}_{-0.01}$	$0.95^{+0.01}_{-0.01}$	4.01 ± 0.28
A2631	$0.25^{+0.09}_{-0.11}$	$12.5^{+2.99}_{-2.69}$	23.2 ± 8.04
A1758N	$0.02^{+0.02}_{-0.01}$	$24.4^{+1.95}_{-2.20}$	15.3 ± 5.20
A1576	$0.35^{+0.07}_{-0.03}$	$7.29^{+0.70}_{-0.72}$	13.4 ± 3.11
A697	$0.20^{+0.08}_{-0.03}$	$11.0^{+1.89}_{-1.75}$	5.41 ± 1.24
RXJ0439.0+0715[a]	$0.78^{+0.04}_{-0.04}$	$3.30^{+0.23}_{-0.21}$	5.42 ± 2.30
RXJ0437.1+0043[a]	$0.83^{+0.05}_{-0.06}$	$1.96^{+0.11}_{-0.09}$	6.25 ± 2.24
A611	$0.72^{+0.04}_{-0.03}$	$2.93^{+0.17}_{-0.19}$	6.38 ± 1.19
Zw3146[a]	$1.01^{+0.01}_{-0.01}$	$0.82^{+0.01}_{-0.01}$	3.25 ± 0.31
Zw7215	$0.13^{+0.25}_{-0.04}$	$12.7^{+1.78}_{-1.66}$	31.5 ± 12.5
A781	$0.03^{+0.18}_{-0.02}$	$32.1^{+19.1}_{-12.7}$	59.2 ± 3.94
A2552	$0.50^{+0.07}_{-0.08}$	$4.92^{+0.62}_{-0.53}$	5.02 ± 1.38

[a]Clusters in the RCC sample (see Section 3.5).

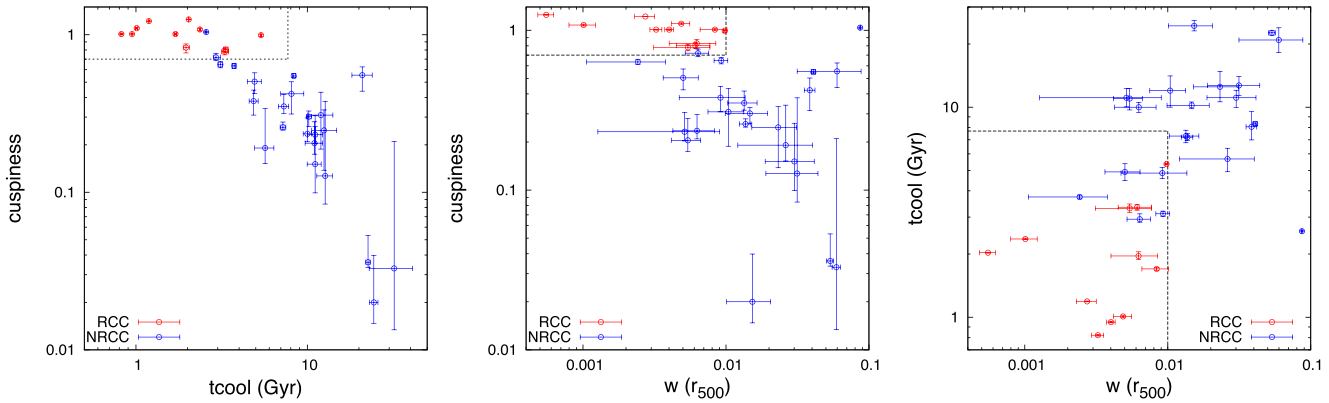

Figure 2. Left: plot of $t_{\rm cool}$ against $\langle w \rangle$ with the dashed horizontal line the cut at $t_{\rm cool} = 6.5$ and the dashed vertical line the cut at $\langle w \rangle = 0.009 r_{500}$, Middle: plot of cuspiness against $\langle w \rangle$ with the dashed horizontal line the cut at cuspiness $= 0.65$ and the dashed vertical line the cut at $\langle w \rangle = 0.009 r_{500}$, Right: plot of cuspiness against $t_{\rm cool}$ with the dashed horizontal line the cut at cuspiness $= 0.65$ and the dashed vertical line the cut at $t_{\rm cool} = 6.5$. The red open circles represent the RCC clusters, and blue open squares represent the NRCC clusters. The cluster at $\langle w \rangle = 0.087$ is the double cool-core cluster A115.

We next determine which clusters in our sample contain a CC. In a comprehensive study, Hudson et al. (2010) tested 16 CC probes, and concluded that for high-quality data a direct measurement of the CCT is the preferred probe. Many of the clusters within our sample have high-quality data and a reliable measurement of the CCT can be obtained. However, for lower quality data, the cuspiness of the gas density profile is the preferred choice. We utilize both of these probes to derive our CC subsample of clusters.

To derive the CCT of our clusters, we use the equation given in Sarazin (1988),

$$t_{\rm cool} = 8.5 \times 10^{10}\ {\rm yr} \left(\frac{n_{\rm p}}{10^{-3}}\right)^{-1} (0.079 k T_{\rm CCT})^{1/2}, \quad (6)$$

where $n_{\rm p} = \sqrt{(1.17 n_{\rm p} n_{\rm e})}$, and $n_{\rm p} n_{\rm e}$ is measured using the best-fitting gas density models given in Section 3.2. $kT_{\rm CCT}$ is measured by extracting a spectrum within [0–0.048]r_{500} (the radius defined in Hudson et al. 2010) and fitted with an absorbed APEC model and the addition of the background model from Section 2. As in Section 3.3, the temperature errors were transformed via the method of Andreon (2012). The errors on $t_{\rm cool}$ were derived from lognormal randomizations centred on the $kT_{\rm CCT}$ and within the transformed error bars determined from the spectral fit. Cuspiness is defined as the logarithmic slope of the gas density profile at a radius of $0.04 r_{500}$, and is modelled using the best-fitting gas density models (Section 3.2). We note that while the errors on both $t_{\rm cool}$ and cuspiness reflect the statistical quality of the data, they may be underestimated due to the assumption of a parametric form of the gas density profile.

In order to determine which clusters in our sample contained a CC, we used the cuts defined in Hudson et al. (2010) for the cuspiness and $t_{\rm cool}$ parameters. Clusters in our sample are determined to have a CC if they have a cuspiness value greater than 0.7, and $t_{\rm cool}$ less than 7.7 Gyr. The values of cuspiness and $t_{\rm cool}$ are given in Table 2.

We plot $t_{\rm cool}$ against cuspiness in Fig. 2, left plot, and cuspiness and $t_{\rm cool}$ against $\langle w \rangle$ in the middle and right plots, respectively. In each plot, the RCC sample and NRCC sample are given by the red and blue open circles, respectively, and the cuts in cuspiness, $t_{\rm cool}$ and $\langle w \rangle$ are shown by the black dashed lines. We note that the cluster A611 had residual flaring in the background light curve and therefore the properties of the cluster could only be derived out to a radius of ≈150 arcsec (see Section 4). A reliable hydrostatic mass estimate for this cluster could not be determined, and it was therefore dropped from the RCC sample. Using the cuts described above, we find 10/34 clusters classed as RCC and 24/34 clusters classed as NRCC.

4 NOTES ON INDIVIDUAL CLUSTERS

In this section, we note any peculiarities or points of interest for observations in which we departed from the described analysis process.

A586 – ObsID 530 was rejected due to long, low-level flaring, leaving ObsID 11723.

A665 – We reject ObsID 531 due to large temperature required to fit soft background residuals (0.6 keV). We reject ObsID 3586 due to several periods of high background. We reject ObsID 7700 due to energy filters placed on the observation. This leaves ObsIDs 12286 and 13201, both ≈50 ks observations.

A115 – This cluster is undergoing a major off-axis merger, with two subclusters separated by 300 arcsec (1 Mpc) in projection. Two regions were manually excluded from the analysis to exclude emission from the southern subcluster. Sources were excluded at $\alpha[2000.0] = 00^{\rm h}55^{\rm m}58\overset{\rm s}{.}89$, $\delta[2000.0] = +26^\circ 19' 28\overset{''}{.}45$ and $\alpha[2000.0] = 00^{\rm h}56^{\rm m}03\overset{\rm s}{.}78$, $\delta[2000.0] = +26^\circ 22' 44\overset{''}{.}48$, with radii 182 and 63 arcsec, respectively.

A963 – A temperature of 0.32 keV was used when fitting an APEC model to the soft background residuals.

A1763 – An extended source at $\alpha[2000.0] = 13^{\rm h}34^{\rm m}55\overset{\rm s}{.}29$, $\delta[2000.0] = +40^\circ 57' 22\overset{''}{.}93$, 304 arcsec from the cluster core was manually excluded. The extended emission is likely associated with a known X-ray source (Evans et al. 2010).

A2261 – A small extended source at $\alpha[2000.0] = 17^{\rm h}22^{\rm m}12\overset{\rm s}{.}15$, $\delta[2000.0] = +32^\circ 06' 54\overset{''}{.}0$, 200 arcsec from the cluster core was manually excluded. The extended emission is associated with a known galaxy at a photo-$z = 0.304$ (Hao et al. 2010).

A1682 – ObsID 2344 was rejected due to high-flare periods, leaving ObsID 11725.

A2111 – This cluster has been shown to be undergoing a head-on merger with a subcluster, appearing as a comet-shaped X-ray subcomponent and hotter than the surrounding gas (Wang, Ulmer & Lavery 1997). A region at $\alpha[2000.0] = 15^{\rm h}39^{\rm m}32\overset{\rm s}{.}68$, $\delta[2000.0] = +34^\circ 28' 04\overset{''}{.}79$, 210 arcsec from the cluster core was manually excluded to exclude the emission from the merger.

Zw5247 – ObsID 539 was rejected due to long, low-level flaring, leaving ObsID 11727. This system consists of a binary merger of two clusters of similar mass. Only one redshift is given in Ebeling et al. (1998), corresponding to the position of the southern subcluster. For this reason, the northern subcluster was manually excluded from our analysis using a box region at $\alpha[2000.0] = 12^{\rm h}34^{\rm m}33\overset{\rm s}{.}18$, $\delta[2000.0] = +09^{\circ}49'52\overset{''}{.}84$ of length 428 × 421 arcsec.

A267 – ObsID 3580 was rejected due to long, low-level flaring leaving ObsID 1448.

A2390 – We discard ObsIDs 500 and 501 as both observations were taken in FAINT mode, which results in poorer background rejection, leaving ObsID 4192. A temperature of 0.25 keV was used when fitting an APEC model to the soft background residuals.

MS1455.0+2232 – For ObsID 4192, we used a temperature of 0.21 keV when fitting an APEC model to the soft background residuals.

Zw5768 – The cluster redshift was given as $z = 0.266$ in Ebeling et al. (2000). This was found to be incorrect, with Böhringer et al. (2000) reporting a spectroscopic redshift of $z = 0.171$. To check this, we searched the SDSS DR7 release (Aihara et al. 2011), and found the redshift of the brightest cluster galaxy of the cluster to be $z = 0.172$. With this updated redshift, the BCS flux for the cluster corresponds to a luminosity well below the limit used to define our sample, and so this cluster was dropped from our analysis.

A1758N – ObsId 7710 was excluded due to energy filters placed on the observation and residual flaring in the observation. ObsID 2213 was excluded due to large residual flaring in the observation. The cluster A1758S was excluded manually from the analysis, using a circle region centred at $\alpha[2000.0] = 13^{\rm h}32^{\rm m}32\overset{\rm s}{.}04$, $\delta[2000.0] = +50^{\circ}24'32\overset{''}{.}95$.

RXJ0439.0+0715 – We excluded the first 6 ks of the observation of ObsID 3583 due to flaring.

A611 – We excluded the first 22 ks of the observation due to long, low-level flaring. Periods of high background were still present in the observation and therefore the cluster temperature was extracted out to a radius of ≈150 arcsec, and this was assumed to be the average cluster temperature ($kT = 8.41^{+0.93}_{-0.75}$ keV). The cluster properties were then extracted within a radius of r_{500} determined following the procedure outlined in Section 3.1, with the temperature fixed at the value above.

Zw3146 – For ObsID 9371, we used a temperature of 0.26 keV when fitting an APEC model to the soft background residuals.

A2552 – ObsID 3288 was rejected due to high-flare periods, leaving ObsID 11730. An extended source, identified as the galaxy cluster NSCS J231153+034038 at $z = 0.36$ (Lopes et al. 2004), at $\alpha[2000.0] = 23^{\rm h}11^{\rm m}48\overset{\rm s}{.}3$, $\delta[2000.0] = +03^{\circ}40'47\overset{''}{.}1$, 276 arcsec from the cluster core was manually excluded.

5 X-RAY SCALING RELATIONS

Establishing the relationship between total mass and observable quantities is a critical step for the derivation of cosmological parameters using galaxy clusters. Cluster properties such as the X-ray luminosity, gas mass, temperature and the Y_X parameter (the product of the gas mass and temperature) provide useful proxies for cluster mass, via the use of well-calibrated scaling relations. In this work, we focus on the scaling of the luminosity with mass. We investigate the form of the *LM* relation, focusing on the sample relation (not accounting for biases), and the bias-corrected relation. The scaling relations are split between the relaxed and unrelaxed subsamples defined in Section 3.5. The X-ray parameters of our clusters are listed in Table 3.

Table 3. X-ray properties of our cluster sample. The properties are derived within r_{500} determined from the hydrostatic mass analysis (see Section 3.4).

Cluster	$r_{\rm H,\,500}$ (Mpc)	$L_{\rm CXO}$ (10^{44} erg s^{-1})	$L_{\rm bol}$ (10^{44} erg s^{-1})	$M_{\rm H}$ (10^{14} M$_\odot$)
A2204[a]	$1.38^{+0.03}_{-0.03}$	16.74 ± 0.06	43.77 ± 0.16	$8.55^{+0.59}_{-0.48}$
RXJ1720.1+2638[a]	$1.36^{+0.11}_{-0.07}$	9.69 ± 0.10	23.70 ± 0.25	$8.20^{+2.13}_{-1.21}$
A586	$1.11^{+0.13}_{-0.07}$	5.46 ± 0.13	13.37 ± 0.32	$4.49^{+1.75}_{-0.81}$
A1914	$1.52^{+0.14}_{-0.11}$	11.92 ± 0.13	38.88 ± 0.43	$11.50^{+3.54}_{-2.28}$
A665	$1.70^{+0.02}_{-0.03}$	8.38 ± 0.06	24.08 ± 0.18	$16.37^{+0.67}_{-0.93}$
A115	$1.13^{+0.01}_{-0.02}$	5.60 ± 0.04	12.43 ± 0.08	$4.85^{+0.17}_{-0.25}$
A520	$1.33^{+0.02}_{-0.02}$	7.04 ± 0.03	19.14 ± 0.09	$8.00^{+0.36}_{-0.28}$
A963	$1.11^{+0.04}_{-0.03}$	6.74 ± 0.07	15.93 ± 0.17	$4.75^{+0.53}_{-0.41}$
A1423[a]	$1.09^{+0.06}_{-0.04}$	5.25 ± 0.08	12.05 ± 0.19	$4.42^{+0.71}_{-0.53}$
A773	$1.38^{+0.12}_{-0.06}$	7.07 ± 0.11	20.48 ± 0.31	$9.12^{+2.59}_{-1.13}$
A1763	$1.42^{+0.15}_{-0.11}$	8.23 ± 0.13	24.00 ± 0.38	$10.01^{+3.59}_{-2.14}$
A2261	$1.25^{+0.08}_{-0.04}$	11.38 ± 0.13	31.65 ± 0.36	$6.89^{+1.41}_{-0.71}$
A1682	$1.13^{+0.09}_{-0.07}$	4.36 ± 0.11	10.93 ± 0.28	$5.02^{+1.29}_{-0.84}$
A2111	$1.23^{+0.12}_{-0.04}$	4.67 ± 0.09	12.65 ± 0.24	$6.46^{+2.02}_{-0.74}$
Zw5247	$0.94^{+0.12}_{-0.07}$	2.76 ± 0.12	6.17 ± 0.26	$2.90^{+1.15}_{-0.59}$
A267	$0.99^{+0.15}_{-0.08}$	5.89 ± 0.22	12.74 ± 0.49	$3.37^{+1.76}_{-0.76}$
A2219	$1.51^{+0.04}_{-0.02}$	17.11 ± 0.12	59.16 ± 0.42	$12.14^{+0.94}_{-0.51}$
A2390	$1.61^{+0.10}_{-0.05}$	18.93 ± 0.10	57.04 ± 0.31	$14.81^{+3.00}_{-1.48}$
Zw2089[a]	$0.94^{+0.15}_{-0.07}$	6.19 ± 0.10	11.22 ± 0.18	$2.96^{+1.67}_{-0.65}$
RXJ2129.6+0005[a]	$1.22^{+0.10}_{-0.07}$	9.68 ± 0.10	22.78 ± 0.25	$6.42^{+1.78}_{-1.04}$
A1835[a]	$1.50^{+0.05}_{-0.04}$	22.68 ± 0.08	60.98 ± 0.21	$12.23^{+1.40}_{-1.05}$
A68	$1.15^{+0.19}_{-0.12}$	6.64 ± 0.20	20.97 ± 0.62	$9.30^{+2.46}_{-1.42}$
MS1455.0+2232[a]	$1.06^{+0.04}_{-0.03}$	11.00 ± 0.09	22.60 ± 0.17	$4.33^{+0.57}_{-0.32}$
A2631	$1.28^{+0.11}_{-0.07}$	8.06 ± 0.14	22.38 ± 0.40	$7.68^{+2.15}_{-1.15}$
A1758	$1.64^{+0.20}_{-0.10}$	8.79 ± 0.10	25.06 ± 0.30	$16.19^{+7.40}_{-2.83}$
A1576	$1.19^{+0.11}_{-0.06}$	6.16 ± 0.10	17.62 ± 0.28	$6.29^{+1.98}_{-0.92}$
A697	$1.55^{+0.21}_{-0.13}$	13.40 ± 0.26	45.61 ± 0.87	$13.85^{+6.47}_{-3.18}$
RXJ0439.0+0715[a]	$1.17^{+0.11}_{-0.07}$	7.36 ± 0.13	17.72 ± 0.30	$5.56^{+1.71}_{-0.92}$
RXJ0437.1+0043[a]	$1.17^{+0.13}_{-0.06}$	7.71 ± 0.12	19.11 ± 0.29	$5.88^{+2.13}_{-0.93}$
A611	$1.12^{+0.15}_{-0.06}$	6.79 ± 0.13	19.15 ± 0.37	$5.36^{+2.45}_{-0.92}$
Zw3146[a]	$1.27^{+0.37}_{-0.17}$	20.55 ± 0.12	50.19 ± 0.30	$8.85^{+1.74}_{-1.09}$
Zw7215	$1.33^{+0.08}_{-0.06}$	5.00 ± 0.19	13.39 ± 0.51	$7.69^{+9.00}_{-2.67}$
A781	$1.13^{+0.07}_{-0.05}$	5.34 ± 0.10	13.25 ± 0.25	$6.89^{+1.07}_{-0.95}$
A2552	$1.22^{+0.08}_{-0.07}$	9.03 ± 0.18	26.99 ± 0.53	$6.90^{+1.49}_{-1.13}$

[a]Relaxed clusters.

5.1 The sample $L_{\rm CXO}$–$M_{\rm H}$ relation

Here we derive the *LM* relation for our clusters. Due to the relative ease of measuring the X-ray luminosity of clusters, scaling relations involving the luminosity have had a rich history (e.g. Mitchell, Ives & Culhane 1977; Arnaud & Evrard 1999; Reiprich & Böhringer 2002; Pratt et al. 2009; Maughan et al. 2012). Fig. 3 shows the derived $L_{\rm CXO}$–$M_{\rm H}$ relation (where $M_{\rm H}$ is the mass derived from the hydrostatic mass analysis) split between the relaxed (red open circles) and unrelaxed (blue open squares) subsamples. The luminosities are derived in the [0–1]r_{500} range for consistency with the comparison to the bias-corrected $L_{\rm CXO}$–$M_{\rm H}$ relation (see Section 5.3).

We fit to the data a power-law relation of the form

$$E(z)^{-\gamma_{LM}}\left(\frac{L_{\rm CXO}}{L_0}\right) = A_{LM}\left(\frac{M_{\rm H}}{M_0}\right)^{B_{LM}}, \quad (7)$$

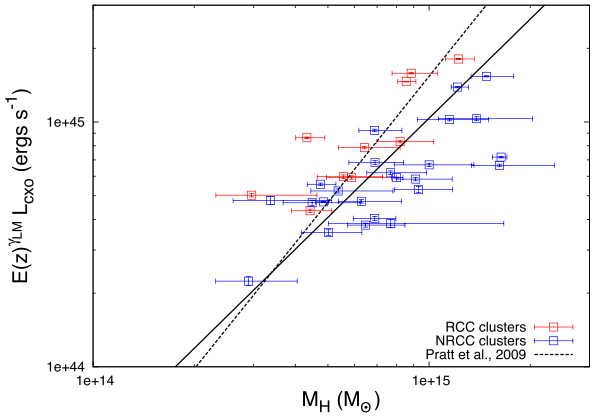

Figure 3. The $L_{\rm CXO}$–$M_{\rm H}$ relation for our clusters, with the masses derived from the relaxed $M_{\rm H}$–T relation. The clusters are split between the relaxed (red open squares) and unrelaxed (blue open squares) samples. The corresponding BCES fit (see Section 5.1) to all the clusters (RCC and NRCC) is given by the black dashed line (sec Section 5.1). The *LM* relation of Pratt et al. (2009) is given by the dot–dashed cyan line.

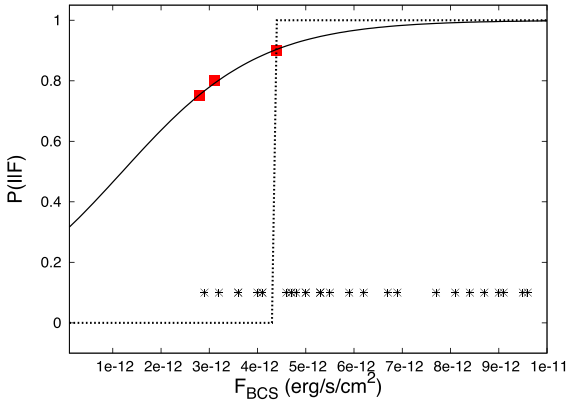

Figure 4. Our logistic function approximation to the (e)BCS completeness as a function of (e)BCS flux is plotted with the published completeness values for the (e)BCS survey (red squares). The asterisk symbols indicate the F_{BCS} of the clusters in our sample, and are at arbitrary completeness. The dotted line represents a step function used to test a limiting case of the selection function (see Section 6.3).

assuming $L_0 = 10^{45}$ erg s^{-1}, $M_0 = 10^{15}\,{\rm M}_\odot$ and $\gamma_{LM} = 2$. Note that the expected self-similar value of γ_{LM} depends on the energy band in which the luminosities are measured. The use of $\gamma_{LM} = 2$ is appropriate for soft-band (0.1–2.4 keV) luminosities (Ettori 2015). The power law was fitted to the data using the BCES orthogonal regression in log space (Akritas & Bershady 1996). We find a normalization and slope of $A_{LM} = (1.82 \pm 0.66) \times 10^{45}$ erg s^{-1} and $B_{LM} = 1.42 \pm 0.60$ for the relaxed sample, and $A_{LM} = (0.92 \pm 0.13) \times 10^{45}$ erg s^{-1} and $B_{LM} = 1.16 \pm 0.27$ for the unrelaxed sample. We find that the normalization of the unrelaxed sample is 1.19 ± 0.09 times lower than that of the relaxed sample (significant at the 1.3σ level); however, this is unsurprising due to the large increase in luminosity towards the centres of CC clusters. We compare to the *LM* relation given in Pratt et al. (2009), appropriate for core-included luminosities in the 0.1–2.4 keV band (see table A.2 in Pratt et al. 2009). The Pratt et al. (2009) *LM* relation is given by the dash–dotted cyan line in Fig. 3. Although the Pratt et al. (2009) *LM* relation appears somewhat steeper than our $L_{\rm CXO}$–$M_{\rm H}$, the difference is only significant at the 1.3σ level.

5.2 Selection function

The sample was selected to match that in Dahle (2006), who selected the clusters from the (e)BCS in the redshift range $0.150 < z < 0.303$ based on the soft-band (0.1–2.4 keV) luminosity as measured in the BCS, $L_{\rm BCS}^{\rm EdS} > 10^{45}$ erg s^{-1}. However (as we indicate with the EdS superscript), the BCS luminosities were computed assuming an Einstein–de Sitter cosmology ($\Omega_{\rm M} = 1, \Omega_\Lambda = 0$, $H_0 = 50$ km s^{-1} Mpc^{-1}), so in order to work in our preferred Λ cold dark matter (ΛCDM) cosmology, it was necessary to convert the BCS luminosities and our selection function to this cosmology. The ΛCDM selection function $L_{\rm lim}(z)$ is well approximated by $L_{\rm BCS} > 5.26 \times 10^{44} \times 10^{0.324z}$ erg s^{-1}, where $L_{\rm BCS}$ (i.e. without an EdS superscript) indicates the soft-band BCS luminosity in our ΛCDM cosmology.

The completeness of the BCS survey is a function of flux, but the full selection function has not been published. However, completeness estimates at specific fluxes are given in Ebeling et al. (1998, 2000), and so we modelled the survey completeness as a logistic function of the form

$$P(I|f) = \left(1 + {\rm e}^{-0.7(f-1.2)}\right)^{-1}, \quad (8)$$

where $P(I|f)$ is the probability that a cluster with a normalized (e)BCS 0.1–2.4 keV flux $f = F_{\rm BCS}/(10^{-12}$ erg s$^{-1})$ is included in the sample. The numerical constants in this model were determined from a simple fit by eye of the logistic function to the published (e)BCS completeness values, as illustrated in Fig. 4. This functional approximation is within 0.01 in $P(I|f)$ of the published completeness values. We show in Section 6.3 that our results are not sensitive to the details of the assumed model for the selection function.

5.3 The bias-corrected $L_{\rm CXO}$–$M_{\rm H}$ relation

The preceding fit of the observed $L_{\rm CXO}$–$M_{\rm H}$ relation (Section 5.1) represents an accurate description of the correlation between luminosity and mass for our subsample. However, in order to compute an unbiased estimate of the population $L_{\rm CXO}$–$M_{\rm H}$ relation, care must be taken to avoid the effects of selection biases (see Allen et al. 2011, for a discussion). Our analysis is based closely on that of M10a, which presents the most complete treatment of selection biases in X-ray cluster surveys and their effects on scaling relations and cosmological studies.

One way to visualize the steps required to correct for the selection biases is to consider how one would realistically generate a synthetic population like that being studied. In our case, the steps would be (i) to use a model mass function $\phi = {\rm d}N/{\rm d}M\,{\rm d}V$ to predict the number of clusters as a function of mass and redshift in the volume studied; (ii) to then generate a Poissonian realization of that population, and assign each cluster a luminosity $L_{\rm BCS}$ based on its mass and redshift, according to a model *LM* relation; (iii) next, intrinsic scatter at the appropriate level (a lognormal with standard deviation δ_{LM}) would be added to the assigned L values; (iv) fluxes could then be computed for each cluster, using assumptions about the temperature and metal abundance (and their mass dependence) to allow k-correction of the fluxes into the observed frame ($F_{\rm BCS}$); (v) statistical scatter would then be added to those luminosities and fluxes, requiring a model predicting the size of the statistical error for a given flux (e.g. by converting the flux to number of counts for a mean exposure time, and assuming Poisson errors); (vi) finally, the sample selection would be applied, rejecting all clusters fainter

than $L_{\rm lim}(z)$, and discarding clusters probabilistically as a function of their flux according to $P(I|f)$. At stage (v), secondary observations (such as our *Chandra* follow-up observations) can be generated by computing a *Chandra* luminosity with its own statistical uncertainty, and possibly including a cross-calibration scaling between *ROSAT* and *Chandra*.

Considering this procedure for simulating data with properties close to the true population gives insight into the likelihood function of the data (the probability of the data being observed given a model and its parameter values). For the *LM* relation, the final likelihood thus depends on the likelihood of the number of clusters detected in the subsample (and by extension the number omitted) and the likelihood of the detected clusters having their observed properties. In the following sections, we derive the likelihood for the *LM* relation and describe our specific implementation of this in fitting to our sample.

5.3.1 *The likelihood function for the LM relation*

The number of clusters predicted by our model to be observed in the subsample defined by our selection function is the integral of the mass function over the volume over the survey, weighted by the probability that a cluster of a given mass would be included in the subsample given the *LM* relation and the intrinsic and statistical scatter on the luminosity. Following M10a and using the notation that observed quantities are denoted with a hat, this is expressed as

$$\begin{aligned}\langle N_{\rm det}\rangle = &\int {\rm d}M \int {\rm d}z\, \phi(M,z)\frac{{\rm d}V}{{\rm d}z\,{\rm d}\Omega}\Omega \\ &\times \int {\rm d}L_{\rm BCS}\, P(L_{\rm BCS}|M) \\ &\times \int {\rm d}\hat{L}_{BCS}\, P(\hat{L}_{BCS}|L_{\rm BCS})P(I|\hat{L}_{BCS},z), \end{aligned} \quad (9)$$

where Ω is the survey area. In this expression, the first probability $P(L_{\rm BCS}|M)$ is the probability that a cluster of mass M has some intrinsically scattered luminosity $L_{\rm BCS}$ (so is a function of our $L_{\rm CXO}$–$M_{\rm H}$ relation parameters A_{LM}, B_{LM}, δ_{LM}). The second probability $P(\hat{L}_{BCS}|L_{\rm BCS})$ is the probability that a cluster of luminosity $L_{\rm BCS}$ would be observed to have a luminosity $\hat{L}_{BCS}$, and so depends on a model of the measurement error on a cluster of arbitrary luminosity. The measurement error is expected to be dominated by counting statistics, but a direct conversion from luminosity to flux to counts would require an exposure time, which is not uniform across the survey. Instead, we derived an empirical function to predict the measurement error on a cluster of given flux by fitting a power law to the measurement errors of the (e)BCS fluxes as a function of flux. The best-fitting relation had the form

$$\frac{\sigma_F}{F_0} = 0.49\left(\frac{F_{BCS}}{F_0}\right)^{0.53} \quad (10)$$

with the normalization factor $F_0 = 10^{-12}$ erg s^{-1} cm^{-2}. The observed scaling is thus very close to the square-root scaling expected for Poisson errors.

The final probability in equation (9), $P(I|\hat{L}_{BCS},z)$, is the probability that a cluster with an observed BCS luminosity $\hat{L}_{BCS}$ at a redshift z would be included in the subsample. This is a combination of the step function associated with $L_{\rm lim}(z)$, and $P(I|f)$ describing the BCS completeness. Note that in principle, the probability of inclusion should depend on T in addition to $\hat{L}_{BCS}$ and z, since the k-correction for the flux is temperature dependent. However, since the BCS luminosities were estimated from *ROSAT* fluxes without temperature measurements, a reference *LT* relation was used to provide the temperature for the k-correction. Since our inclusion probability must match as closely as possible the BCS completeness function, we use the same method to k-correct $L_{\rm BCS}$ when estimating f for the selection function (equation 8), which removes the T dependence.

The likelihood of a cluster in our sample having the observed properties $(\hat{L}_{BCS}, \hat{L}_{CXO}, \hat{M})$ is given by

$$\begin{aligned}P(\hat{L}_{BCS},\hat{L}_{CXO},\hat{M}|I,z) = &\int {\rm d}M \int {\rm d}L_{\rm BCS}\, \frac{\phi(M,z)}{\langle N\rangle} \\ &\times P(L_{\rm BCS}|M)P(\hat{L}_{BCS}|L_{\rm BCS}) \\ &\times P(\hat{L}_{CXO}|L_{\rm BCS})P(\hat{M}|M). \end{aligned} \quad (11)$$

The quantity $\langle N\rangle$ is the total number of clusters predicted by the model, and is given by the integral of the mass function ϕ over the mass range of interest, and normalizes the mass function to a probability distribution for an arbitrary cluster to have a mass M at redshift z. We note that $\langle N\rangle$ is not a parameter of our model, but is a useful parameter to monitor. $P(L_{\rm BCS}|M)$ is as defined above, and the remaining terms are the probability of each of the observables, using the measured uncertainty for that observable. Here we have treated each of the observables as independent, although in principle a covariance will exist between $\hat{L}_{CXO}$ and $\hat{M}$ as the luminosity is determined within an aperture derived from the observed mass. In practice, this effect will be weak as the luminosity is centrally concentrated and is insensitive to the precise choice of aperture. The joint probability of the full set of observed cluster properties is the product of $P(\hat{L}_{BCS},\hat{L}_{CXO},\hat{M})$ over all $N_{\rm det}$ observed clusters in the sample. Note that we neglect any observational uncertainty on z.

M10a showed that the final likelihood for the sample of clusters and their observed properties is the product of a Poisson likelihood of N total (detected plus undetected) clusters given the model prediction $\langle N\rangle$, a binomial coefficient accounting for the number of ways of drawing $N_{\rm det}$ detected clusters from the total N, the joint probability of the set of observed cluster properties [the product of equation (11) over the $N_{\rm det}$ clusters] and the probability of not detecting the remaining $N - N_{\rm det}$ clusters. Neglecting terms not dependent on the model parameters, the likelihood simplifies to

$$P(\hat{L}_{BCS},\hat{L}_{CXO},\hat{M},z) \propto {\rm e}^{-\langle N_{\rm det}\rangle}\prod_{i=1}^{N_{\rm det}}\left\langle\tilde{n}_{{\rm det},i}\right\rangle, \quad (12)$$

where

$$\left\langle\tilde{n}_{{\rm det},i}\right\rangle = P(\hat{L}_{BCS},\hat{L}_{CXO},\hat{M})\,\langle N\rangle \quad (13)$$

for the ith cluster.

5.3.2 *Implementation and nuisance parameters*

With the likelihood in equation (12), and priors on the model parameters, we can compute the posterior probability distribution for each parameter using standard Markov chain Monte Carlo (MCMC) techniques. Our final set of model parameters consists of those parameters describing the $L_{\rm CXO}$–$M_{\rm H}$ relation (A_{LM},B_{LM},δ_{LM}), each of which was assigned uniform priors, along with a nuisance parameter described below (naturally marginalized over in the MCMC procedure).

A cross-calibration factor $X_{\rm cal}$ describing the uncertainty in the calibration between *Chandra* and *ROSAT* fluxes was introduced as a nuisance parameter in the model. $X_{\rm cal}$ is defined as the ratio

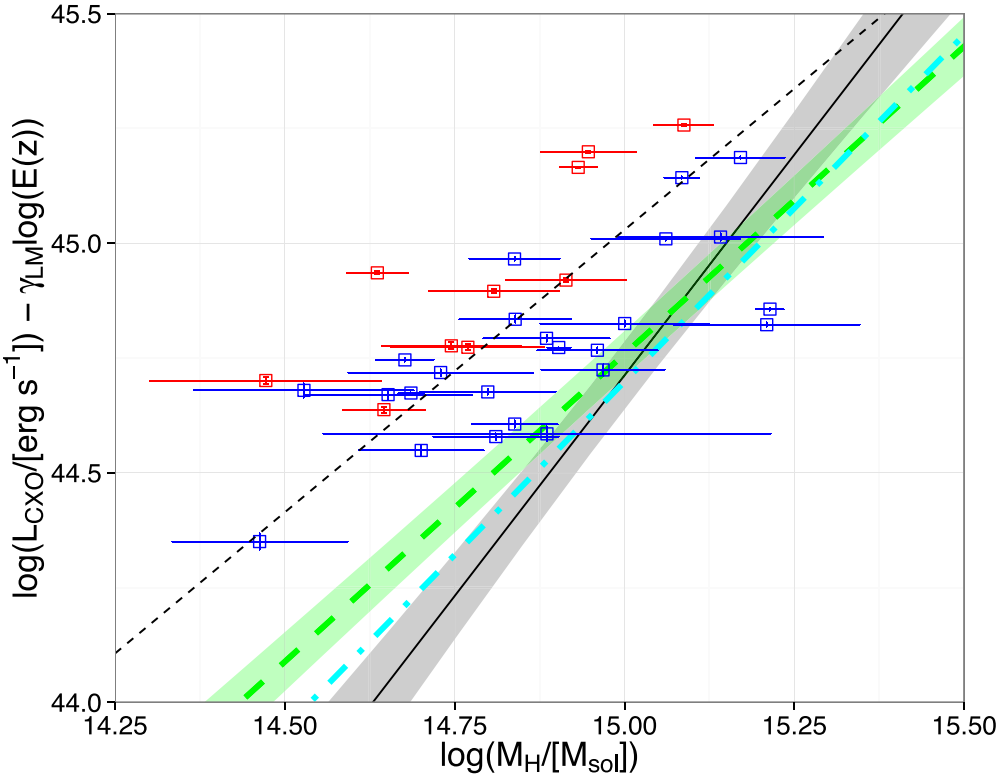

Figure 5. $L_{\rm CXO}$–$M_{\rm H}$ relation with best-fitting model. The open squares show the $L_{\rm CXO}$ luminosities split between the relaxed (red) and unrelaxed (blue) clusters, calibrated to *ROSAT* reference using the calibration factor $X_{\rm cal}$. Our best-fitting model is shown as the solid black line with the grey shading indicating the 1σ uncertainty. The bold dashed green line and shaded region indicate the best-fitting *LM* relation for the 'all data' sample of M10b with its 1σ uncertainty, scaled by a factor of 1.10 to scale the *ROSAT* PSPC luminosities used in M10b on to our *Chandra* reference (see Section 5.3.3). The bold cyan dash–dotted indicates the best-fitting *LM* relation for the BCS-only sample of M10b (see Section 6.1).

of the *Chandra* flux measured within r_{500} to F_{BCS}. This parameter thus encompasses several factors: cross-calibration between *ROSAT* and *Chandra* fluxes; a mean aperture correction from r_{500} to the 1.43 Mpc radius to which the (e)BCS fluxes were extrapolated; and exclusion of point sources in *Chandra* data that may have been unresolved or only partially excluded in the *ROSAT* data. We assigned a weak prior to $X_{\rm cal}$, using a lognormal distribution with mean 0 and standard deviation of 1 in natural log space, i.e. a 100 per cent uncertainty, although the results are insensitive to this choice, $X_{\rm cal}$ is well constrained by the data.

The analysis also requires a mass function to describe the cluster number density (above some threshold mass), and for this we used the mass function of Tinker et al. (2008). In our analysis, we have treated all cosmological parameters as constant, and we take the same approach with the mass function, using a tabulated mass function produced by *HMFcalc* (Murray, Power & Robotham 2013) for our *WMAP*9 cosmology with a virial mass M_{500c} (the mass r_{500} with respect to the critical density of the Universe). We have fixed all cosmological parameters since we are focusing on the scaling relations, and do not expect useful cosmological constraints from our sample. Fixing the cosmological and mass function parameters means that our scaling relations are not marginalized over the uncertainties in those parameters, and should be regarded as estimates for a fixed cosmology [in contrast, the combined cosmology and scaling relation study of Mantz et al. (2010b) does include cosmological and mass function parameters in the analysis].

Our final model thus consists of three parameters describing the *LM* relation (A_{LM},B_{LM},δ_{LM}), and the nuisance parameter $X_{\rm cal}$ describing the conversion between F_{BCS} and F_{CXO}.

Our fits were performed using the R statistical computing environment,[4] and the posterior probability distribution was analysed using the Bayesian inference package *Laplace's Demon*[5] within R, which contains many MCMC algorithms. The fits were performed with a lower bound flux cut of 10^{12} erg s^{-1} cm^{-2} (i.e. the lower bound of the integration), corresponding to the count rate cut of 0.07 counts s^{-1} employed in Ebeling et al. (1998). The best-fitting model parameters are described by the mean and standard deviation of the posterior probability distribution, as estimated from the MCMC chain after excluding the start of the chain before the parameter values became stationary.

5.3.3 *The L_{CXO}–M_H relation*

The $L_{\rm CXO}$–$M_{\rm H}$ relation is plotted in Fig. 5, and the best-fitting parameters are given in Table 4, which include the uncertainty due to that on $X_{\rm cal}$ (which has a best-fitting value of $X_{\rm cal} = 1.094 \pm 0.002$). The posterior probability distributions of the model parameters and the correlations between parameters are shown in Fig. 6. This figure also illustrates that the $X_{\rm cal}$ parameter is not degenerate with the parameters of interest.

We compare to the BCES fit outlined in Section 5.1, given by the black dashed line in Fig. 5. The difference between the two fitting methods is visibly striking, with the normalization of the fit when accounting for selection effects 2.2 ± 0.4 times lower

[4] http://www.r-project.org/
[5] http://www.bayesian-inference.com/software

Table 4. Best-fitting parameters for the *LM* relations modelled here. For the fits performed using the M10a method, the *LM* relations were modelled in the soft band, with the *Chandra* luminosities calibrated to the *ROSAT* luminosities by the $X_{\rm cal}$ factor (denoted as $L_{\rm BCS}$–$M_{\rm H}$). In the table, we also give the relation calibrated to *Chandra* soft-band luminosities (simply scaling by $X_{\rm cal}$) and *Chandra* bolometric luminosities, by applying a bolometric correction (see Section 5.3.4). These relations are denoted by $L_{\rm CXO}$–$M_{\rm H}$ and $L_{\rm bol}$–$M_{\rm H}$, respectively. δ_{LM} is the intrinsic scatter measured in natural log space so represents a fractional value.

Relation	Method	$r_{\rm H,\,500}$ A_{LM}	B_{LM}	γ_{LM}	δ_{LM}
$L_{\rm CXO}$–$M_{\rm H}$	BCES	1.15 ± 0.15	1.34 ± 0.29	2	0.38 ± 0.07
$L_{\rm BCS}$–$M_{\rm H}$	M10a	0.47 ± 0.08	1.92 ± 0.24	2	0.68 ± 0.11
$L_{\rm CXO}$–$M_{\rm H}$	M10a	0.52 ± 0.09	1.92 ± 0.24	2	0.68 ± 0.11
$L_{\rm bol}$–$M_{\rm H}$	M10a	1.45 ± 0.24	2.22 ± 0.24	7/3	0.68 ± 0.11

when not taking into account selection effects (significant at the 3.7σ level). This comparison clearly shows the size of the biases on cluster samples selected to have very luminous clusters, such as the LoCuSS (Zhang et al. 2008) and CCCP (Mahdavi et al. 2013) cluster samples, and is an extreme illustration of the importance of modelling selection biases. We also compare to the *LM* relation given in Mantz et al. (2010b, hereafter M10b), which uses the method outlined in M10a to account for selection effects. This comparison is discussed further in Section 6.1.

5.3.4 *The L_{bol}–M_H relation*

So far we have been considering the scaling of soft-band luminosity with mass, but it is often useful to refer to the bolometric luminosity $L_{\rm bol}$. It is not possible to fit our model directly to bolometric luminosities, since the selection function is defined in terms of the soft-band luminosity. Instead, we can convert the $L_{\rm CXO}$–$M_{\rm H}$ relation to an $L_{\rm bol}$–$M_{\rm H}$ relation by using a bolometric correction.

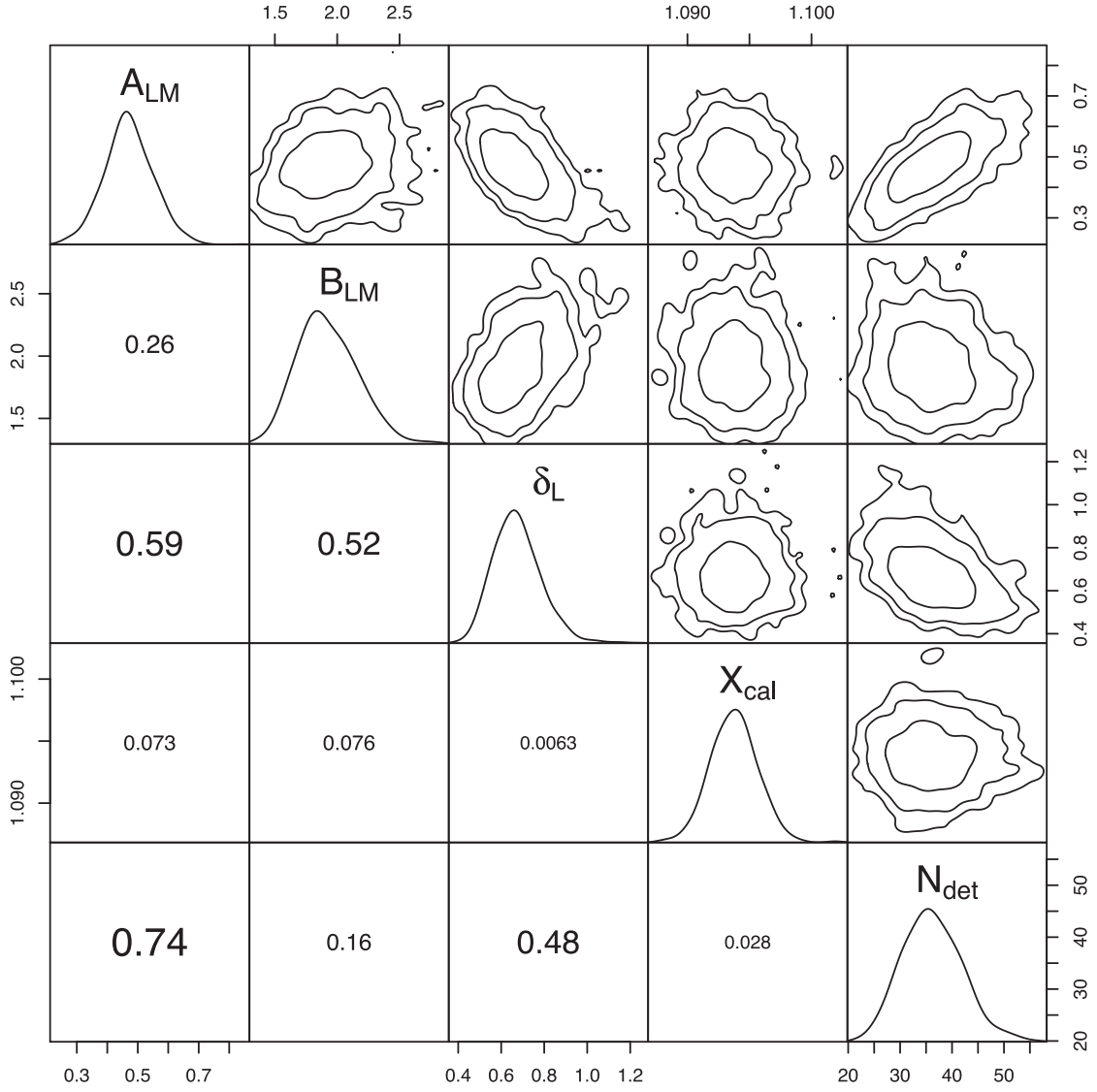

Figure 6. Correlation matrix of the $L_{\rm CXO}$–$M_{\rm H}$ relation model. The posterior densities are shown along the diagonal, with 1σ, 2σ and 3σ confidence contours for the pairs of parameters shown in the upper triangle panels. The lower triangle panels show the Pearson's correlation coefficient for the corresponding pair of parameters (with a text size proportional to the correlation strength).

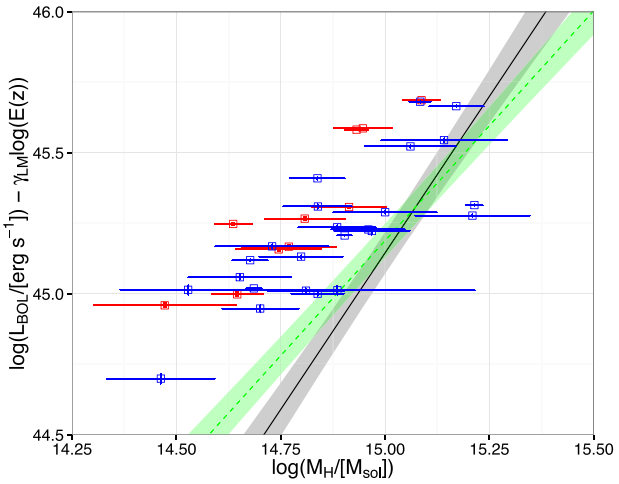

Figure 7. $L_{\rm bol}$–$M_{\rm H}$ relation with best-fitting model. The open squares show the $L_{\rm bol}$ luminosities, split between the relaxed (red) and unrelaxed (blue) clusters. Our best-fitting model is shown as the solid black line with grey shading indicating the 1σ uncertainty (transformed from the $L_{\rm CXO}$–$M_{\rm H}$ using the corrections outlined in Section 5.3.4). The dashed green line and shaded region indicate the best-fitting bolometric *LM* relation for the 'all data' sample of M10b with its 1σ uncertainty.

Using XSPEC simulations, we find that this correction can be approximated by

$$\frac{L_{\rm bol}}{L_{\rm CXO}} = A_{\rm bol}\left(\frac{T}{T_0}\right)^{B_{\rm bol}} \tag{14}$$

with $A_{\rm bol} = 2.08$ and $B_{\rm bol} = 0.54$ for $T_0 = 5$ keV, giving bolometric luminosities accurate to $\lesssim$3 per cent across the range 3–15 keV. Combined with a temperature–mass (*TM*) relation of the form

$$\frac{T}{T_0} = A_{TM}E(z)^{\gamma_{TM}}\left(\frac{M}{M_0}\right)^{B_{TM}} \tag{15}$$

then the bolometric *LM* relation becomes

$$\begin{aligned}\frac{L_{\rm bol}}{L_0} &= E(z)^{\gamma_{LM}+B_k\gamma_{TM}}A_{LM}A_{\rm bol}A_{TM}^{B_{\rm bol}}\left(\frac{M}{M_0}\right)^{B_{LM}+B_{\rm bol}B_{TM}}\\ &= E(z)^{\gamma_{LM,\rm bol}}A_{LM,\rm bol}\left(\frac{M}{M_0}\right)^{B_{LM,\rm bol}}.\end{aligned} \tag{16}$$

Note that the self-similar evolution of the *TM* relation alters the evolution of the bolometric $L_{\rm bol}$–$M_{\rm H}$ relation from that of the soft-band $L_{\rm CXO}$–$M_{\rm H}$ relation.

To derive the $L_{\rm bol}$–$M_{\rm H}$ relation, we used the *TM* relation presented in Section 6.3. The $L_{\rm bol}$–$M_{\rm H}$ relation is shown in Fig. 7, with the best-fitting model coefficients given in Table 4. The uncertainties on the model parameters include correlated uncertainties on A_{LM}, B_{LM} and $X_{\rm cal}$ from the posterior chains of the MCMC analysis, and the uncertainty on the slope and normalization of the *TM* relation, treating those as independent. This is justified since there is not a strong covariance between the *TM* and *LM* relations (M10b; Maughan 2014).

6 DISCUSSION

6.1 Comparison with M10b

Fig. 5 shows the best-fitting relation of the 'all data' sample of M10b. This relation was derived from a sample of 238 clusters at $z < 0.5$ and with *ROSAT* luminosities for all clusters, with *Chandra* follow-up observations providing luminosities and masses (estimated from the gas mass) for a subset of 66 objects. This *LM* relation was derived as part of a cosmological analysis (which includes non-cluster cosmological data to constrain their derived cosmological parameters), rather than having cosmological parameters fixed as in our analysis. In spite of these differences, the M10b *LM* relation is the most suitable comparison for our work as it is the only other example of an *LM* relation with full corrections for selection biases.

The luminosities in M10b were calibrated to a *ROSAT* PSPC reference, so in order to compare with our $L_{\rm CXO}$–$M_{\rm H}$ relation, we derived a calibration of the M10b luminosities on to our *Chandra* reference by comparing luminosities for 24 objects in common between the samples. We found a low-scatter correlation between the values, with the M10b luminosities higher by a factor of 1.10 on average. This difference is in the opposite sense to that found in M10b, where *Chandra* luminosities (using CALDB 4.1.2) were found to be 14 per cent higher than PSPC luminosities. This difference is due to the evolving *Chandra* calibration (we used CALDB 4.6.2), and systematic differences in the analyses. We do not pursue these calibration differences further, but simply scale the M10b *LM* relation normalization by a factor of 1.10 and note that this difference is typical of cross-calibration uncertainties in X-ray telescope effective areas (Nevalainen, David & Guainazzi 2010). With this scaling in place, we find a reasonably good agreement between the relations, with the slope of our relation being steeper at the 2.4σ level.

One might expect a better agreement between the relations since (a) the fit method used in this work is based upon that used in M10a, and (b) our sample contains 24 clusters in common with the M10b sample. We investigate this difference by first comparing the masses of the 24 clusters in common, noting that M10b use the gas mass as a proxy for cluster mass. We find that the masses of the clusters in common are entirely consistent (when fitting a power-law relation with the slope fixed at unity). The scatter between the mass estimates is 22 ± 5 per cent, which is consistent with the larger scatter we find in the $L_{\rm CXO}$–$M_{\rm H}$ relation compared with that in the M10b L–$M_{\rm Mgas}$ relation. Secondly, the samples that were used is that M10b used clusters drawn from three different parent surveys, while our sample is derived from the (e)BCS. To eliminate this difference, we compared our $L_{\rm CXO}$–$M_{\rm H}$ relation to a version of the M10b *LM* relation derived using only clusters from the (e)BCS survey (Mantz, private communication).

The bold cyan dash–dotted line in Fig. 5 shows the relation based upon using (e)BCS-only clusters in M10b, using the M10a analysis. When these consistent cluster subsets are used, the agreement is improved and the slopes and normalization are both within $\approx 1.5\sigma$.

6.2 Mass comparisons

The sample of clusters presented in this work were also studied in Landry et al. (2013, hereafter L13). We compare here the masses derived in this work to those presented in L13. We note that although this work and L13 use the V06 method to derive cluster masses, the implementation was performed separately. There have also been three updates from the L13 paper, to this work. As stated, we use *WMAP*9 cosmology throughout, whereas L13 use *WMAP*7 ($\Omega_{\rm M} = 0.27$, $\Omega_\Lambda = 0.73$ and $H_0 = 70.2$; Komatsu et al. 2011). The next change is the versions of CIAO and CALDB used in the separate analysis; we have used CIAO 4.6 and CALDB v4.5.9, whereas L13 use CIAO 4.2 and CALDB v4.3.1. Finally, in this work, we used the *C*-statistic in spectral fits, while L13 used the χ^2 statistic with binned spectra.

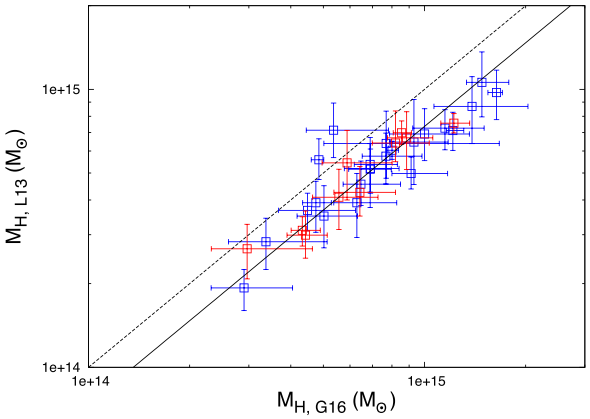

Figure 8. Comparison of the mass estimate determined in this work and those presented in L13. The dashed line represents a 1:1 relation, with the black line a fit to the data assuming a power-law relation with the slope fixed at unity.

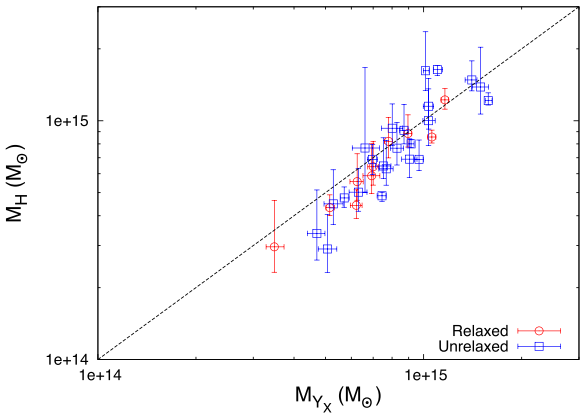

Figure 9. Comparison of the masses calculated via our hydrostatic mass analysis and those calculated via the *YM* relation of Vikhlinin et al. (2009a), split between the relaxed (red open squares) and unrelaxed (blue open squares) samples. The black dashed line represents a 1:1 relationship.

Fig. 8 compares the masses given in L10 to those derived in this work. The black dashed line represents a 1:1 relationship. The black solid line is a fit to the data (using a power law with the slope fixed at unity), where we find that our masses are on average 29 ± 3.0 per cent higher than those in L13. We should note that the masses are not compared within the same radii, but within their respective r_{500}. An analysis of our cluster sample with the same cosmology, CIAO and CALDB versions, and χ^2 statistic yields a 1:1 mass comparison. We investigated the impact of these differences on analysis methods. Changing the cosmology from *WMAP*7 to *WMAP*9 changed r_{500} and M_{500} by ≈1 per cent. The choice of statistic in the spectra fitting had a larger impact. If we used the χ^2 statistic, with spectra grouped to at least 30 counts per bin, the inferred temperatures were systematically lower, and the derived M_{500} were lower by 10 per cent on average. The remaining 20 per cent difference in mass compared to L13 is thus due to the different CIAO/CALDB versions used. There have been several major updates to the CALDB between the two versions used in these studies, and we do not attempt to investigate which are responsible for the observed shift in masses.

We further compare our derived masses to those presented in Martino et al. (2014). Martino et al. (2014) studied a sample of 50 clusters from the LoCuSS cluster sample, calculating masses based on *Chandra* observations and utilizing temperature profiles to calculate hydrostatic masses. Using 21 clusters in common between the LoCuSS sample and the clusters in this work, we find that our masses are 11 ± 5 per cent higher, consistent with our use of the *C*-statistic [Martino et al. (2014) used the χ^2 statistic].

6.3 Systematic effects

6.3.1 Reliability of hydrostatic masses

Throughout this work, we have used masses determined assuming hydrostatic equilibrium of the ICM. However, non-thermal pressure sources associated with bulk and turbulent motions of the cluster gas lead to what is known as the hydrostatic mass bias. Hydrodynamical simulations have shown that these processes can lead to underestimates of the hydrostatic cluster mass by ∼10–30 per cent (e.g. Kay et al. 2004; Jeltema et al. 2008; Lau, Kravtsov & Nagai 2009; Shi & Komatsu 2014). Observationally however, the level of hydrostatic bias is less clear. Several recent studies have attempted to measure the amount of bias by comparing hydrostatic mass estimates to estimates based upon other techniques (e.g. weak lensing, caustics) that are independent of the equilibrium state of the ICM. Some have found evidence for a level of bias similar to that of simulations (e.g. von der Linden et al. 2014; Hoekstra et al. 2015), while others found results consistent with no hydrostatic bias (e.g. Applegate et al. 2016; Maughan et al. 2016; Smith et al. 2016). Intriguingly, Smith et al. (2016) showed that results of von der Linden et al. (2014) and Hoekstra et al. (2015) converged on a low (5–10 per cent) bias when only $z < 0.3$ clusters were used (the same redshift range as our sample).

In addition to the question of an overall hydrostatic bias, we must consider whether the hydrostatic masses will be more biased or scattered relative to the true mass for unrelaxed clusters. Hydrodynamical simulations tend to agree that disturbed clusters show a larger bias than relaxed ones, although disagreements exist over the size of the biases (e.g. Lau et al. 2009; Nelson, Lau & Nagai 2014; Shi et al. 2016). However, for our sample, we find observational evidence that the hydrostatic masses of the unrelaxed clusters are not differently biased than those of the relaxed clusters.

First, in Maughan et al. (2016), we compared the hydrostatic and caustic mass profiles of 16 clusters from the sample studied in this work. The caustic masses are taken from Rines et al. (2013), and are not affected by the dynamical state of the cluster. The comparison implies that the hydrostatic masses cannot be biased low by more than 10 per cent (at the 3σ level), and shows no evidence for a dependence on the dynamical state of the clusters (albeit based on a relatively small subset of clusters).

A second piece of observational evidence that our hydrostatic masses are reliable comes from the comparison to the masses calculated via the Y_X–mass (Y_X–M) relation of Vikhlinin et al. (2009a). Y_X is the product of the gas mass and core-excised temperature measured. Simulations have shown the Y_X parameter to be a low-scatter proxy for cluster mass, regardless of its dynamical state (Kravtsov, Vikhlinin & Nagai 2006); however, observational evidence is so far lacking. None the less, if hydrostatic masses for unrelaxed clusters were significantly affected by biases compared to relaxed clusters, a comparison of hydrostatic masses to Y_X-based masses should highlight this. We iterated on the Y_X–M relation until r_{500} converged, and the masses (M_{Y_X}) were calculated from the Y_X determined within this radius. Fig. 9 shows the resulting comparison of the masses determined from our hydrostatic analysis, used throughout

this work, with M_{Y_X} as described above, split between the relaxed (red open squares) and unrelaxed (blue open squares) clusters. The black dashed line represents a 1:1 relationship. Although the clusters appear to differ slightly from the 1:1 correlation, the data do not exclude a 1:1 relationship.

The resulting mass comparisons for the relaxed and unrelaxed subsamples are in excellent agreement, and both show a similarly low scatter, supporting the idea that our hydrostatic masses are not more biased or scattered for the unrelaxed clusters compared with their relaxed counterparts. A possible reason for this is that the dynamical activity of the clusters is more important in the inner parts of the cluster, while the ICM around r_{500} is close to equilibrium.

Overall, these observational studies support the use of hydrostatic masses as a calibrator of the *LM* relation, but clearly the question of hydrostatic bias remains open and is an important possible source of systematic uncertainty in our results.

6.3.2 *Dependence on cosmological parameters*

Throughout this paper, we have assumed a *WMAP*9 cosmology. Recently however, data from *Planck* have found support for a different cosmology (Planck Collaboration XIII 2016a). Since the cosmology is held fixed in our analysis, this is a source of systematic uncertainty. As stated in Section 6.2, the effect of changing the cosmology is negligible on the measured cluster properties when changing from *WMAP*7 to *WMAP*9. Although the change is larger for the *Planck* cosmology, the derived properties will change only at the 1 per cent level. Therefore, the *LM* relation of the observed clusters will remain largely unchanged. The cosmology will impact more strongly the bias-corrected fitting of the $L_{\rm CXO}$–$M_{\rm H}$ relation. The *Planck* cosmology currently predicts a higher value of σ_8 (the fluctuation amplitude at 8 h^{-1} Mpc) compared to *WMAP*9. An increase in value of σ_8 would lead to an increased number density of clusters in the Universe. In this situation, in order for the model to correctly predict the number of clusters observed in our sample, the underlying cluster population, inferred from the mass function, would have to be less luminous on average for their given mass. This would lead to a lower inferred normalization of the *LM* relation. Incidentally, if the underlying population were on average less luminous, our cluster sample would be more extremely biased, falling further into the tail of the luminosity intrinsic scatter.

6.3.3 *Uncertainty on the selection function*

When modelling the selection function (see Section 5.2), we use three completeness estimates at specific fluxes and model with a logistic function. However, this selection function is likely a simplified form of the true (e)BCS selection function (which is unavailable). We tested our use of the logistic function to model the selection function by considering some limiting cases of the behaviour of $P(I|f)$. For this test, we considered step functions at two different flux cuts. The first step function uses a flux cut calculated from the luminosity of the least luminous cluster in our sample. The second flux cut is taken from the 90 per cent completeness level ($F_{X,\,90\,\rm per\,cent} = 4.4\times\ 10^{-12}$ erg s^{-1} cm^{-2}) as given in Ebeling et al. (1998). We note that $F_{X,\,90\,\rm per\,cent}$ is larger than the eBCS flux limit and thus we remove five clusters from our sample when considering this second step function. The $L_{\rm CXO}$–$M_{\rm H}$ relation modelled using these step functions, and the logistic function used throughout this analysis, are all entirely consistent.

7 SUMMARY AND CONCLUSIONS

Using a statistically complete sample of 34 high-luminosity galaxy clusters, we have derived the X-ray hydrostatic masses of the cluster sample, and investigated the form of the *LM* scaling relation. The form of the relation is fitted using two methods, one using a simple regression fit to the data, and another accounting for selection effects. Our main conclusions are as follows.

(i) Using the CCT, the cuspiness of the gas density profile and the centroid shift, we separate the cluster sample into relaxed CC (relaxed) and NCC (unrelaxed) clusters. We find 10/34 relaxed clusters and 24/34 unrelaxed clusters.

(ii) We derive hydrostatic mass estimates for the cluster sample, irrespective of the dynamical state of the cluster, utilizing gas density and temperature profiles.

(iii) Taking fully into account selection effects, we fit for the soft-band *LM* relation, finding a slope of $B_{LM} = 1.92 \pm 0.24$ and scatter $\delta_{LM} = 0.68 \pm 0.11$. Comparing this relation to one that does not account for selection effects, we find that accounting for selection effects lowers the normalization of the $L_{\rm CXO}$–$M_{\rm H}$ relation by a factor of 2.2 ± 0.4.

(iv) Throughout the analysis, we use the *C*-statistic when fitting cluster spectra. Although the *C*-statistic has been shown to more accurately recover the cluster temperature, the χ^2 statistic has been more commonly employed. Comparing the hydrostatic masses determined using both statistics, we find the *C*-statistic masses are 10 $\pm$ 2.3 per cent higher than those found using the χ^2 statistic.

(v) Testing the use of step functions to model the selection function, we find that the fitted $L_{\rm CXO}$–$M_{\rm H}$ relation is consistent with the relation when using our logistic function to model the selection function.

We have studied a highly biased cluster sample, where the selection has a profound effect on the derived scaling relations. We have shown the importance of taking into account the selection effects when fitting for the observed *LM* scaling relation. This is crucial for the understanding of scaling laws of cluster samples when used for the purposes of cosmology. Current and upcoming cluster surveys (e.g. *XXL*, *Planck*, clusters detected with *e-ROSITA*) will all require a method of determining the cluster mass for cosmological studies. This will most likely come in the form of a mass–observable scaling relation, for which the selection effects will need to be fully accounted for. Furthermore, although high-luminosity clusters are observationally cheaper to follow up in order to derive X-ray hydrostatic masses, and hence the construction of scaling relations, they lead to highly biased cluster samples, as shown throughout this work.

ACKNOWLEDGEMENTS

PG acknowledges support from the UK Science and Technology Facilities Council. We thank A. Mantz for useful discussions and for providing additional fits used in the comparison to his work.

REFERENCES

Aihara H. et al., 2011, ApJS, 193, 29
Akritas M. G., Bershady M. A., 1996, ApJ, 470, 706
Allen S. W., Rapetti D. A., Schmidt R. W., Ebeling H., Morris R. G., Fabian A. C., 2008, MNRAS, 383, 879
Allen S. W., Evrard A. E., Mantz A. B., 2011, ARA&A, 49, 409
Anders E., Grevesse N., 1989, Geochim. Cosmochim. Acta, 53, 197
Andreon S., 2012, A&A, 546, A6

Applegate D. E. et al., 2016, MNRAS, 457, 1522
Arnaud K. A., 1996, in Jacoby G. H., Barnes J., eds, ASP Conf. Ser. Vol. 101, Astronomical Data Analysis Software and Systems V. Astron. Soc. Pac., San Francisco, p. 17
Arnaud M., Evrard A. E., 1999, MNRAS, 305, 631
Bauer F. E., Fabian A. C., Sanders J. S., Allen S. W., Johnstone R. M., 2005, MNRAS, 359, 1481
Bharadwaj V., Reiprich T. H., Lovisari L., Eckmiller H. J., 2015, A&A, 573, A75
Böhringer H. et al., 2000, ApJS, 129, 435
Böhringer H., Chon G., Collins C. A., 2014, A&A, 570, A31
Comis B., de Petris M., Conte A., Lamagna L., de Gregori S., 2011, MNRAS, 418, 1089
Connor T., Donahue M., Sun M., Hoekstra H., Mahdavi A., Conselice C. J., McNamara B., 2014, ApJ, 794, 48
Dahle H., 2006, ApJ, 653, 954
Ebeling H., Edge A. C., Bohringer H., Allen S. W., Crawford C. S., Fabian A. C., Voges W., Huchra J. P., 1998, MNRAS, 301, 881
Ebeling H., Edge A. C., Allen S. W., Crawford C. S., Fabian A. C., Huchra J. P., 2000, MNRAS, 318, 333
Eke V. R., Cole S., Frenk C. S., Patrick Henry J., 1998, MNRAS, 298, 1145
Ettori S., 2015, MNRAS, 446, 2629
Evans I. N. et al., 2010, ApJS, 189, 37
Fruscione A. et al., 2006, in Silva D. R., Doxsey R. E., eds, Proc. SPIE, Vol. 6270, Observatory Operations: Strategies, Processes, and Systems. 62701V
Giles P. A., Maughan B. J., Birkinshaw M., Worrall D. M., Lancaster K., 2012, MNRAS, 419, 503
Hao J. et al., 2010, ApJS, 191, 254
Henry J. P., 1997, ApJ, 489, L1
Henry J. P., Arnaud K. A., 1991, ApJ, 372, 410
Hinshaw G. et al., 2013, ApJS, 208, 19
Hoekstra H., Herbonnet R., Muzzin A., Babul A., Mahdavi A., Viola M., Cacciato M., 2015, MNRAS, 449, 685
Hudson D. S., Mittal R., Reiprich T. H., Nulsen P. E. J., Andernach H., Sarazin C. L., 2010, A&A, 513, A37
Ikebe Y., Reiprich T. H., Böhringer H., Tanaka Y., Kitayama T., 2002, A&A, 383, 773
Jeltema T. E., Hallman E. J., Burns J. O., Motl P. M., 2008, ApJ, 681, 167
Kaiser N., 1986, MNRAS, 222, 323
Kalberla P. M. W., Burton W. B., Hartmann D., Arnal E. M., Bajaja E., Morras R., Pöppel W. G. L., 2005, A&A, 440, 775
Kay S. T., Thomas P. A., Jenkins A., Pearce F. R., 2004, MNRAS, 355, 1091
Komatsu E. et al., 2011, ApJS, 192, 18
Kravtsov A. V., Vikhlinin A., Nagai D., 2006, ApJ, 650, 128
Landry D., Bonamente M., Giles P., Maughan B., Joy M., Murray S., 2013, MNRAS, 433, 2790 (L13)
Lau E. T., Kravtsov A. V., Nagai D., 2009, ApJ, 705, 1129
Le Brun A. M. C., McCarthy I. G., Schaye J., Ponman T. J., 2014, MNRAS, 441, 1270
Lopes P. A. A., de Carvalho R. R., Gal R. R., Djorgovski S. G., Odewahn S. C., Mahabal A. A., Brunner R. J., 2004, AJ, 128, 1017
Lovisari L., Reiprich T. H., Schellenberger G., 2015, A&A, 573, A118
McCarthy I. G., Schaye J., Bower R. G., Ponman T. J., Booth C. M., Dalla Vecchia C., Springel V., 2011, MNRAS, 412, 1965
Mahdavi A., Hoekstra H., Babul A., Bildfell C., Jeltema T., Henry J. P., 2013, ApJ, 767, 116
Mantz A., Allen S. W., Ebeling H., Rapetti D., 2008, MNRAS, 387, 1179
Mantz A., Allen S. W., Rapetti D., Ebeling H., 2010a, MNRAS, 406, 1759 (M10a)
Mantz A., Allen S. W., Ebeling H., Rapetti D., Drlica-Wagner A., 2010b, MNRAS, 406, 1773 (M10b)
Mantz A. B., Allen S. W., Morris R. G., Rapetti D. A., Applegate D. E., Kelly P. L., von der Linden A., Schmidt R. W., 2014, MNRAS, 440, 2077
Mantz A. B., Allen S. W., Morris R. G., Schmidt R. W., von der Linden A., Urban O., 2015, MNRAS, 449, 199
Markevitch M. et al., 2003, ApJ, 583, 70
Martino R., Mazzotta P., Bourdin H., Smith G. P., Bartalucci I., Marrone D. P., Finoguenov A., Okabe N., 2014, MNRAS, 443, 2342
Maughan B. J., 2014, MNRAS, 437, 1171
Maughan B. J., Giles P. A., Randall S. W., Jones C., Forman W. R., 2012, MNRAS, 421, 1583
Maughan B. J., Giles P. A., Rines K. J., Diaferio A., Geller M. J., Van Der Pyl N., Bonamente M., 2016, MNRAS, 461, 4182
Mitchell R. J., Ives J. C., Culhane J. L., 1977, MNRAS, 181, 25P
Mittal R., Hicks A., Reiprich T. H., Jaritz V., 2011, A&A, 532, A133
Murray S., Power C., Robotham A., 2013, Astron. Comput., 3, 23
Nagai D., Kravtsov A. V., Vikhlinin A., 2007, ApJ, 668, 1
Nelson K., Lau E. T., Nagai D., 2014, ApJ, 792, 25
Nevalainen J., David L., Guainazzi M., 2010, A&A, 523, A22
O'Hara T. B., Mohr J. J., Bialek J. J., Evrard A. E., 2006, ApJ, 639, 64
Pacaud F. et al., 2007, MNRAS, 382, 1289
Pacaud F. et al., 2016, A&A, 592, A2
Planck Collaboration XIII, 2016a, A&A, 594, A13
Planck Collaboration XXIV, 2016b, A&A, 594, A24
Poole G. B., Fardal M. A., Babul A., McCarthy I. G., Quinn T., Wadsley J., 2006, MNRAS, 373, 881
Pratt G. W., Croston J. H., Arnaud M., Böhringer H., 2009, A&A, 498, 361
Reiprich T. H., Böhringer H., 2002, ApJ, 567, 716
Rines K., Geller M. J., Diaferio A., Kurtz M. J., 2013, ApJ, 767, 15
Rykoff E. S. et al., 2008, MNRAS, 387, L28
Santos J. S., Tozzi P., Rosati P., Böhringer H., 2010, A&A, 521, A64
Sarazin C. L., 1988, X-ray Emission from Clusters of Galaxies. Cambridge Univ. Press, Cambridge
Sereno M., Ettori S., 2015, MNRAS, 450, 3675
Shi X., Komatsu E., 2014, MNRAS, 442, 521
Shi X., Komatsu E., Nagai D., Lau E. T., 2016, MNRAS, 455, 2936
Short C. J., Thomas P. A., Young O. E., Pearce F. R., Jenkins A., Muanwong O., 2010, MNRAS, 408, 2213
Smith R. K., Brickhouse N. S., Liedahl D. A., Raymond J. C., 2001, ApJ, 556, L91
Smith G. P. et al., 2016, MNRAS, 456, L74
Stanek R., Evrard A. E., Böhringer H., Schuecker P., Nord B., 2006, ApJ, 648, 956
Tinker J., Kravtsov A. V., Klypin A., Abazajian K., Warren M., Yepes G., Gottlöber S., Holz D. E., 2008, ApJ, 688, 709
Vikhlinin A., 2006, ApJ, 640, 710
Vikhlinin A., Markevitch M., Murray S. S., Jones C., Forman W., Van Speybroeck L., 2005, ApJ, 628, 655
Vikhlinin A., Kravtsov A., Forman W., Jones C., Markevitch M., Murray S. S., Van Speybroeck L., 2006, ApJ, 640, 691 (V06)
Vikhlinin A., Burenin R., Forman W. R., Jones C., Hornstrup A., Murray S. S., Quintana H., 2007, in Böhringer H., Pratt G. W., Finoguenov A., Schuecker P., eds, Heating versus Cooling in Galaxies and Clusters of Galaxies. Springer-Verlag, Berlin, p. 48
Vikhlinin A. et al., 2009a, ApJ, 692, 1033
Vikhlinin A. et al., 2009b, ApJ, 692, 1060
von der Linden A. et al., 2014, MNRAS, 443, 1973
Wang Q. D., Ulmer M. P., Lavery R. J., 1997, MNRAS, 288, 702
Weißmann A., Böhringer H., Šuhada R., Ameglio S., 2013, A&A, 549, A19
Zhang Y.-Y., Finoguenov A., Böhringer H., Kneib J.-P., Smith G. P., Kneissl R., Okabe N., Dahle H., 2008, A&A, 482, 451

APPENDIX A: PARAMETERS OF THE GAS DENSITY AND TEMPERATURE PROFILES

Here we give the parameters of the gas density and temperature profiles of the cluster sample. Tables A1 and A2 list the individual parameters of the fits to the gas density and temperature profiles, respectively.

Table A1. Table listing the individual parameters of the fit to the gas density profile for each of the clusters in our sample.

Cluster	n_0 10^{-3} cm^{-3}	r_c (kpc)	r_s (kpc)	α	β	ϵ
A2204[a]	24.579	67.778	1363.850	2.028	0.532	3.095
RXJ1720.1+2638[a]	36.927	47.171	695.129	0.781	0.542	1.088
A586	16.085	51.421	161.327	0.001	0.323	1.837
A1914	14.004	154.980	2703.460	0.000	0.718	5.000
A665	11.249	67.700	1367.420	0.000	0.397	5.000
A115	29.314	29.186	3967.680	0.668	0.445	5.000
A520	3.408	391.718	339.217	0.000	0.685	0.760
A963	10.907	96.634	997.588	0.898	0.518	3.384
A1423[a]	20.548	39.845	1632.000	0.330	0.446	3.257
A773	8.315	138.667	846.138	0.000	0.552	1.365
A1763	7.557	133.460	1351.600	0.000	0.500	2.582
A2261	13.171	114.317	2382.670	0.922	0.587	1.629
A1682	2.593	278.998	3046.010	0.757	0.610	0.000
A2111	4.753	190.063	1061.220	0.161	0.602	0.000
Z5247	0.954	396.838	1905.930	1.051	0.423	5.000
A267	9.892	134.225	3333.110	0.000	0.655	0.106
A2219	5.995	216.035	331.133	0.507	0.300	2.250
A2390	68.229	18.435	579.989	0.000	0.368	2.878
Z2089[a]	18.299	71.553	142.615	1.751	0.628	0.000
RXJ2129.6+0005[a]	9.959	116.326	1760.560	1.800	0.566	5.000
A1835[a]	100.000	27.147	469.409	0.368	0.483	1.531
A68	5.240	259.711	665.144	0.416	0.783	0.000
MS1455.0+2232[a]	13.548	106.649	100.000	1.865	0.411	1.412
A2631	3.634	370.272	2472.830	0.453	0.819	0.000
A1758	2.903	798.833	399.279	0.000	0.300	3.855
A1576	10.987	89.185	1191.130	0.000	0.501	1.913
A697	8.734	170.861	923.611	0.000	0.548	1.609
RXJ0439.0+0715[a]	1.483	799.982	200.646	1.552	0.701	1.641
RXJ0437.1+0043[a]	44.707	20.610	198.695	0.000	0.353	1.558
A611	2.274	735.655	130.495	1.353	0.433	1.886
Z7215	5.550	190.280	1148.840	0.000	0.647	0.000
Z3146[a]	11.306	163.032	3984.170	1.866	0.705	0.000
A781	2.684	466.725	234.173	0.000	0.403	1.674
A2552	8.841	88.866	244.596	0.837	0.300	1.778

[a]Relaxed clusters.

Table A2. Table listing the individual parameters of the fit to the temperature profile for each of the clusters in our sample.

Cluster	T_0 (keV)	r_{cool} (kpc)	T_{min} (keV)	r_t (kpc)	a_{cool}	a	b	c
A2204[a]	12.366	20.585	2.857	984.922	4.754	−0.110	5.000	3.827
RXJ1720.1+2638[a]	18.601	10.014	0.128	345.408	0.000	−0.292	4.124	0.478
A586	9.316	50.020	3.474	235.606	0.193	0.176	1.790	0.000
A1914	13.170	15.105	2.296	251.379	0.491	0.228	1.082	0.026
A665	10.608	45.354	2.095	225.281	0.990	0.049	1.208	0.007
A115	16.326	499.984	1.793	500.000	0.069	−0.372	4.830	0.711
A520	13.118	10.000	4.416	489.086	0.385	−0.183	2.121	0.843
A963	18.020	74.065	0.187	356.107	0.004	−0.151	4.999	1.000
A1423[a]	12.929	15.525	1.672	317.779	3.000	−0.359	0.881	0.802
A773	14.577	89.707	3.520	188.148	0.000	0.057	1.685	0.000
A1763	9.235	10.009	5.975	474.620	0.538	0.018	0.475	0.000
A2261	12.661	51.410	6.000	499.973	0.587	−0.081	2.294	0.708
A1682	22.910	125.064	4.997	174.871	3.000	0.000	0.609	0.609
A2111	11.559	35.705	0.239	292.874	1.834	0.004	0.000	0.000
Z5247	14.303	1.000	14.303	100.003	0.000	−0.292	0.663	0.663
A267	10.243	1.000	10.243	499.933	0.000	−0.180	1.000	1.000
A2219	21.601	36.384	6.000	499.996	0.277	−0.106	1.253	0.556
A2390	23.223	36.957	1.705	860.371	0.225	−0.206	9.744	1.500
Z2089[a]	8.146	151.381	2.217	153.531	1.472	0.068	5.000	0.304
RXJ2129.6+0005[a]	9.984	53.821	2.133	428.921	0.755	−0.038	5.000	0.614
A1835[a]	13.290	24.435	3.050	1403.660	4.994	−0.171	3.340	3.655
A68	10.915	1.000	10.915	499.955	0.000	−0.047	3.596	0.829
MS1455.0+2232[a]	9.797	11.262	5.913	495.920	0.000	−0.211	1.335	0.573
A2631	15.474	10.001	4.642	248.360	0.741	−0.056	0.726	0.476
A1758	8.606	77.399	5.039	215.501	0.896	−0.153	0.601	0.014
A1576	12.311	36.027	2.215	218.731	1.114	0.079	1.131	0.281
A697	17.424	36.662	2.560	234.165	0.001	−0.047	1.415	0.000
RXJ0439.0+0715[a]	11.448	34.978	4.274	499.998	0.000	−0.059	5.000	0.853
RXJ0437.1+0043[a]	14.097	55.522	5.437	499.921	0.049	−0.234	1.027	0.438
A611	8.105	26.170	0.100	470.611	3.000	0.056	5.000	0.484
Z7215	14.172	1.000	14.172	158.818	0.000	−0.139	0.000	0.000
Z3146[a]	21.039	227.673	3.502	499.998	0.332	−0.257	1.542	0.840
A781	10.321	1.000	10.321	500.000	0.000	−0.287	2.219	0.999
A2552	15.305	17.238	1.818	234.280	0.009	−0.006	0.948	0.000

[a]Relaxed clusters.

APPENDIX B: FIT STATISTICS

Here we provide further information on the parameters of the L_{CXO}–M_H relation. Fig. B1 plots the posterior densities for parameters of the L_{CXO}–M_H relation, with shaded regions highlighting regionsenclosing 68 per cent, 95 per cent and 99.7 per cent of the distribution. The vertical line in each plot represents the median. Table B1 gives the medians and values enclosing 68 per cent, 95 per cent and 99.7 per cent of the distribution for parameters of the L_{CXO}–M_H relation.

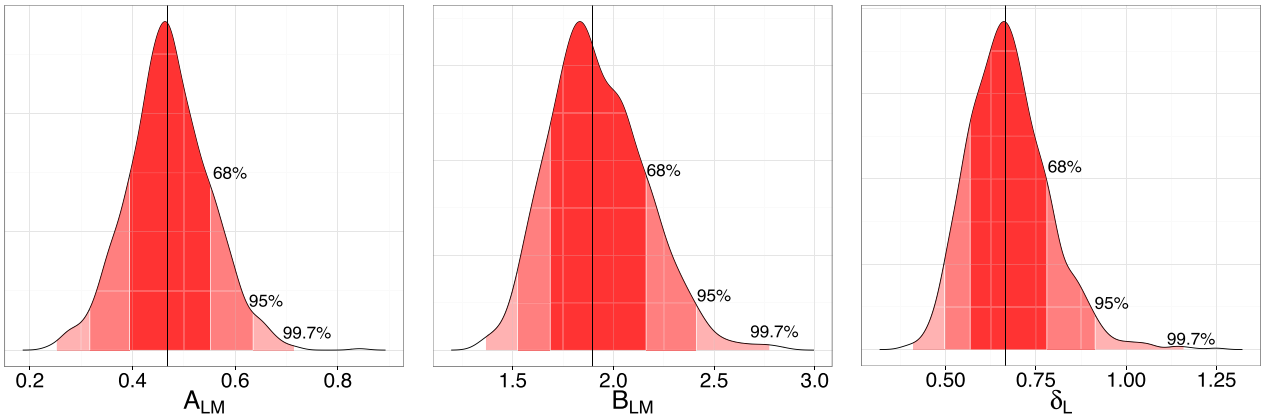

Figure B1. Plots showing the posterior densities of the fit parameters of the L_{CXO}–M_H relation, with the left, middle and right plots showing the normalization (A_{LM}), slope (B_{LM}) and scatter (δ_{LM}), respectively. The shaded regions in each plot represent the regions enclosing 68 per cent, 95 per cent and 99.7 per cent of the distribution, centred on the median, with the vertical line representing the median.

Table B1. Table listing the median and values enclosing 68 per cent, 95 per cent and 99.7 per cent of the distribution for parameters of the L_{CXO}–M_H relation.

Parameter	Median	68 per cent	95 per cent	99.7 per cent
A_{LM}	0.47	0.39–0.55	0.32–0.63	0.25–0.71
B_{LM}	1.90	1.69–2.16	1.53–2.41	1.37–2.78
δ_{LM}	0.67	0.57–0.78	0.50–0.91	0.41–1.16

APPENDIX C: IMAGES, GAS DENSITY AND TEMPERATURE PROFILES

Here we show images, gas density and temperature profiles for our cluster sample. Fig. C1 shows an adaptively smoothed image of the cluster measuring 3×3 Mpc on a side (left), the emissivity profile with the best-fitting gas density profile (middle) and the temperature profile (right) with the best-fitting three-dimensional model (red) and the corresponding projected profile (blue) for the cluster A2204. Figs C2–C33 show the rest of the cluster sample.

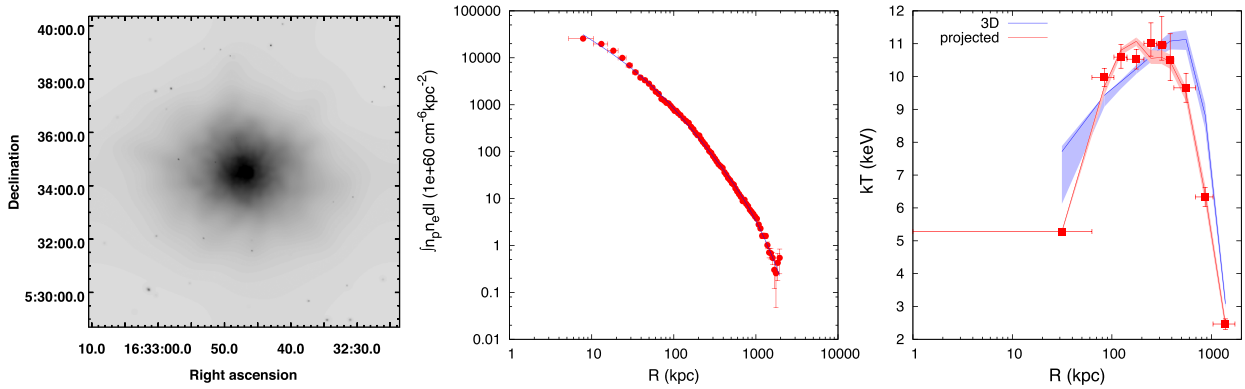

Figure C1. Left: an adaptively smoothed image of the cluster A2204 (3×3 Mpc on a side). Centre: observed projected emissivity profile for A2204, with the best-fitting gas density profile shown by the solid blue line. Right: temperature profile for A2204. The solid red line shows the best-fitting three-dimensional model to the temperature profile, and the solid blue line represents the corresponding projected profile. The red and blue shaded regions show the corresponding uncertainties on the three-dimensional model and projected profile, respectively, and obtained from Monte Carlo simulations.

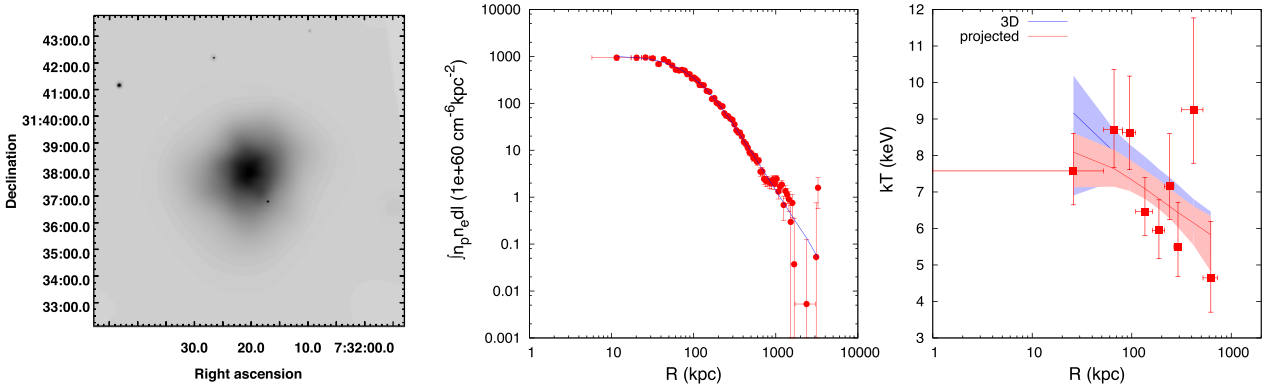

Figure C2. Same as Fig. C1 but for A586.

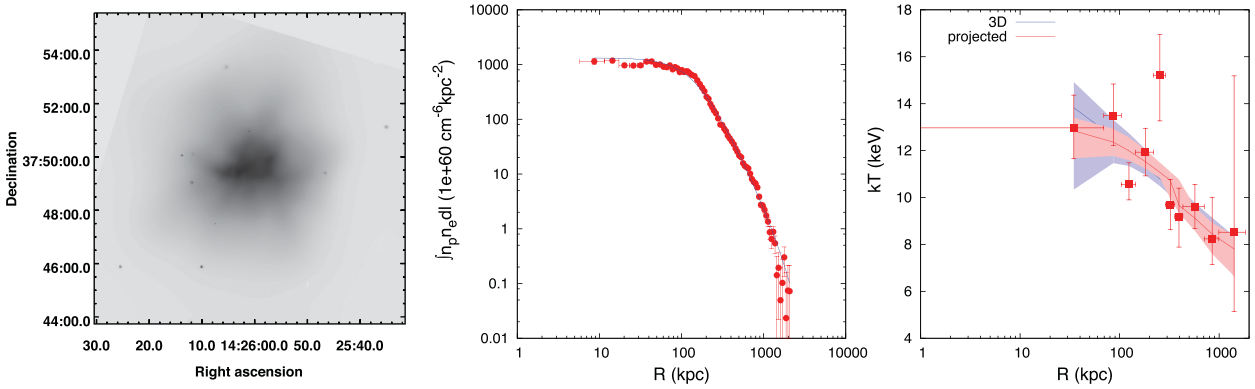

Figure C3. Same as Fig. C1 but for A1914.

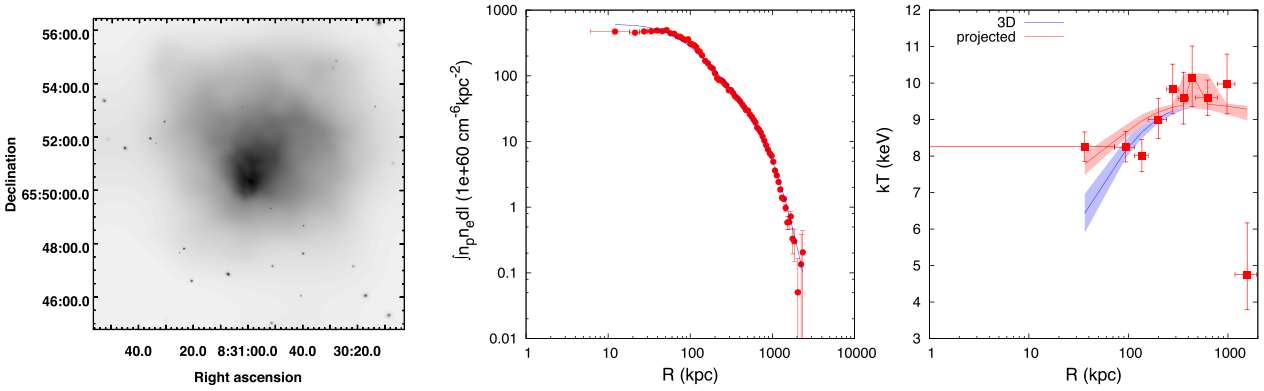

Figure C4. Same as Fig. C1 but for A665.

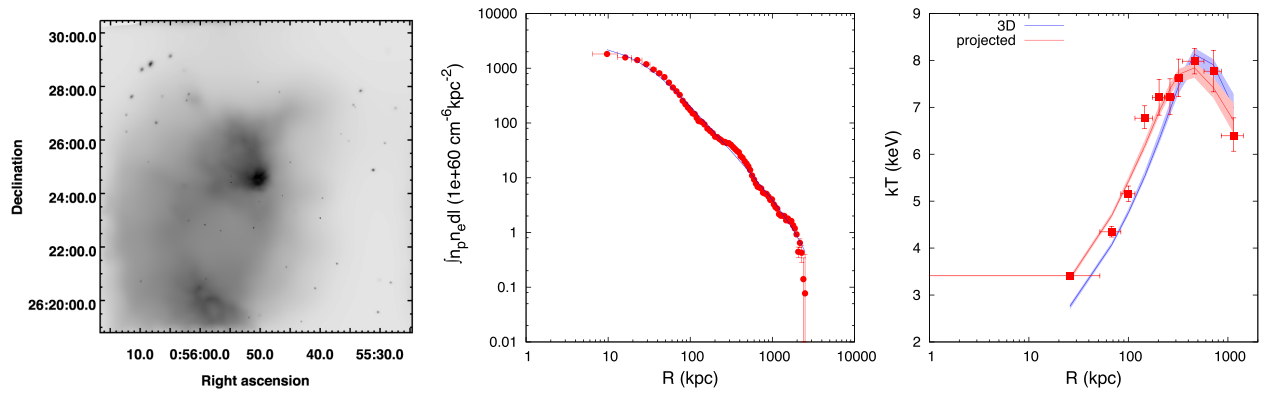

Figure C5. Same as Fig. C1 but for A115.

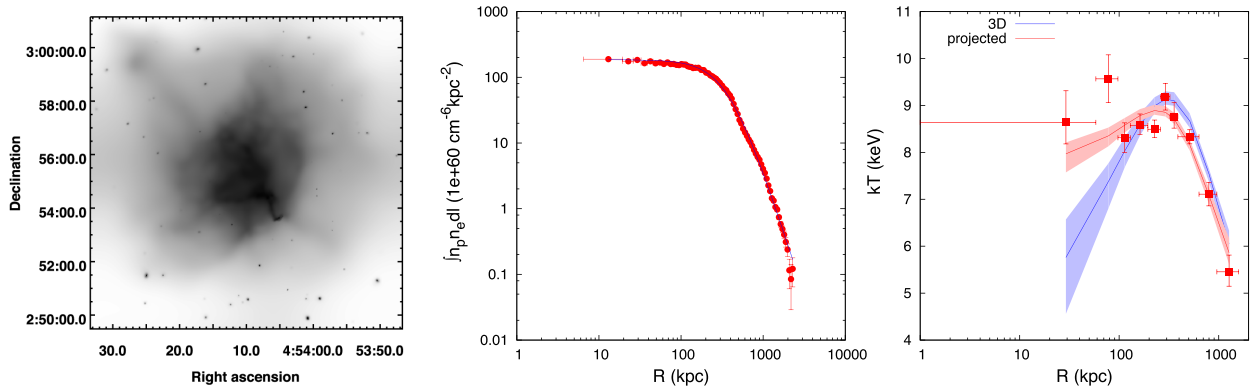

Figure C6. Same as Fig. C1 but for A520.

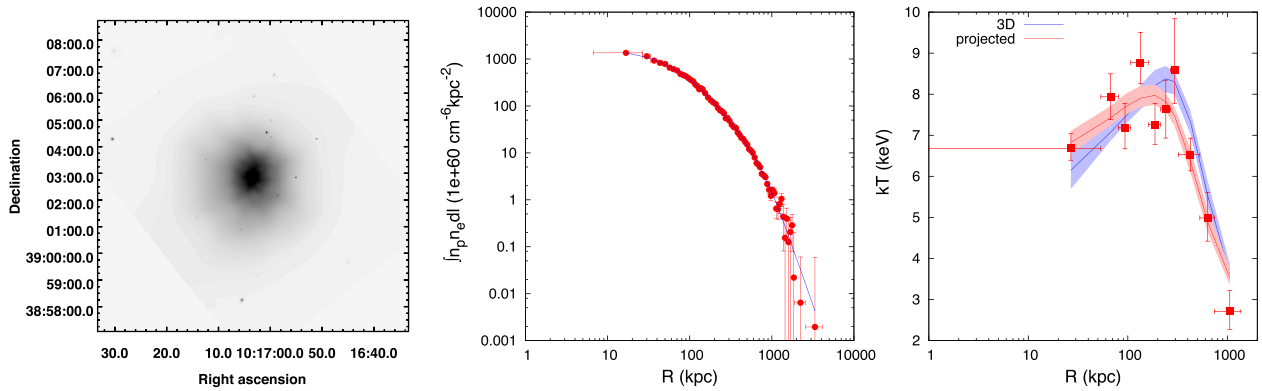

Figure C7. Same as Fig. C1 but for A963.

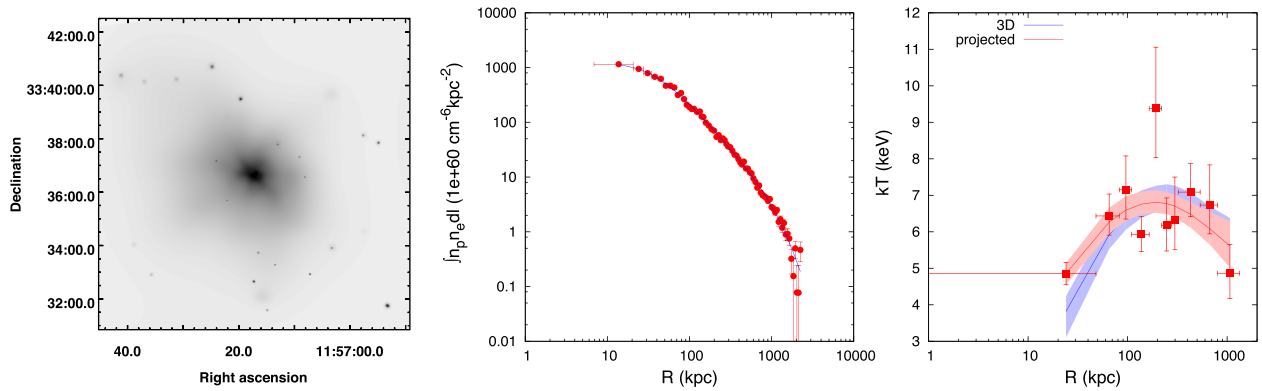

Figure C8. Same as Fig. C1 but for A1423.

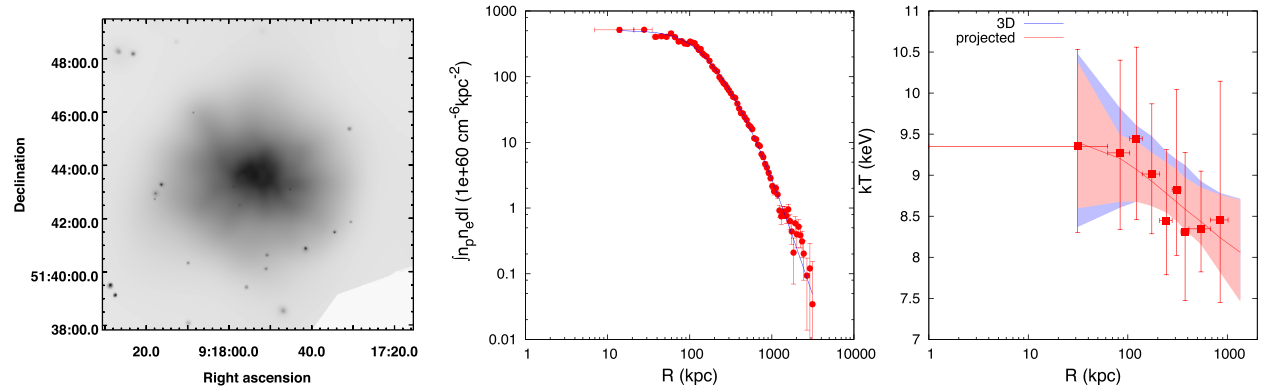

Figure C9. Same as Fig. C1 but for A773.

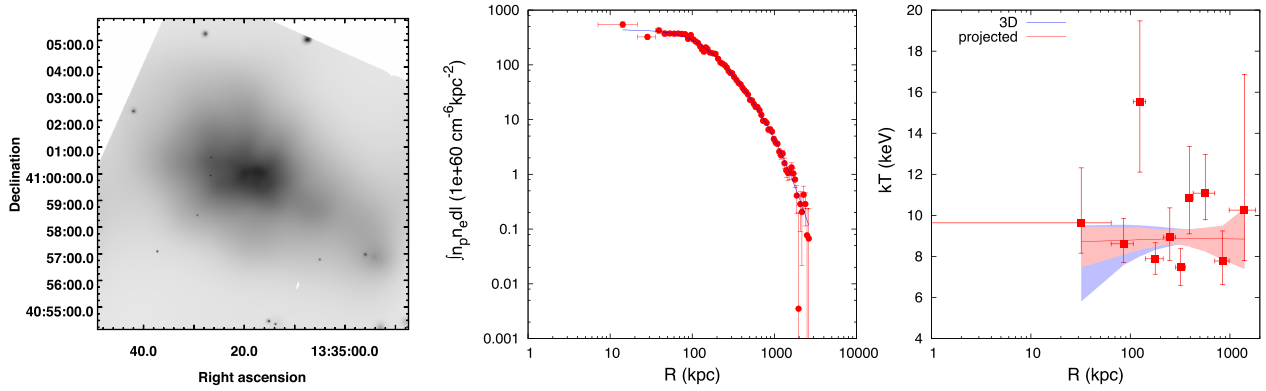

Figure C10. Same as Fig. C1 but for A1763.

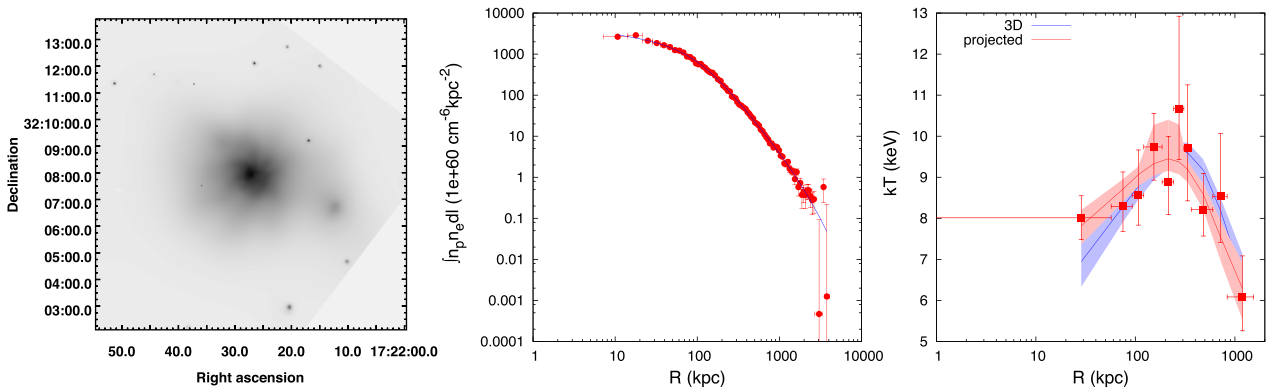

Figure C11. Same as Fig. C1 but for A2261.

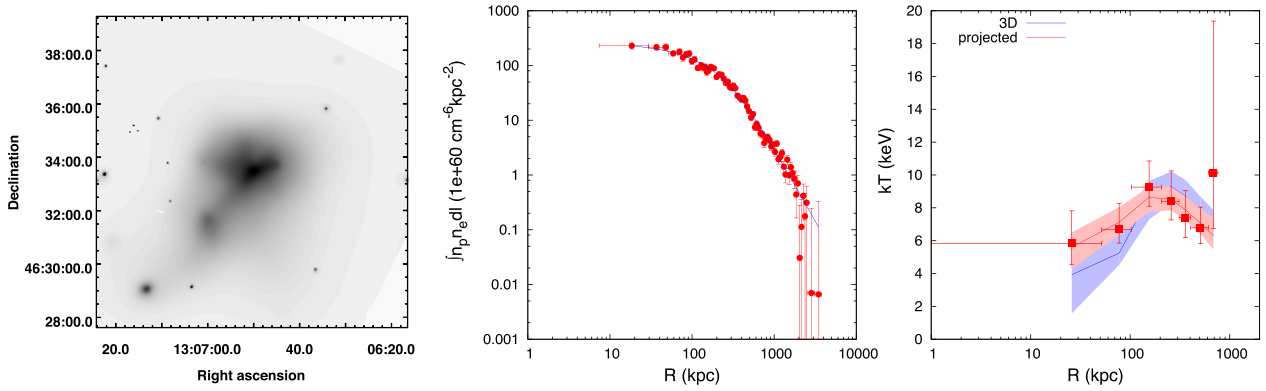

Figure C12. Same as Fig. C1 but for A1682.

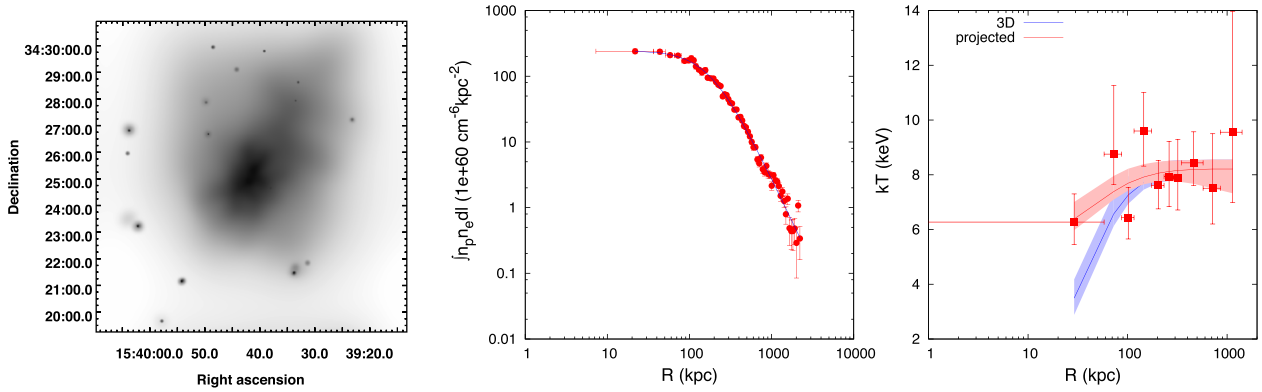

Figure C13. Same as Fig. C1 but for A2111.

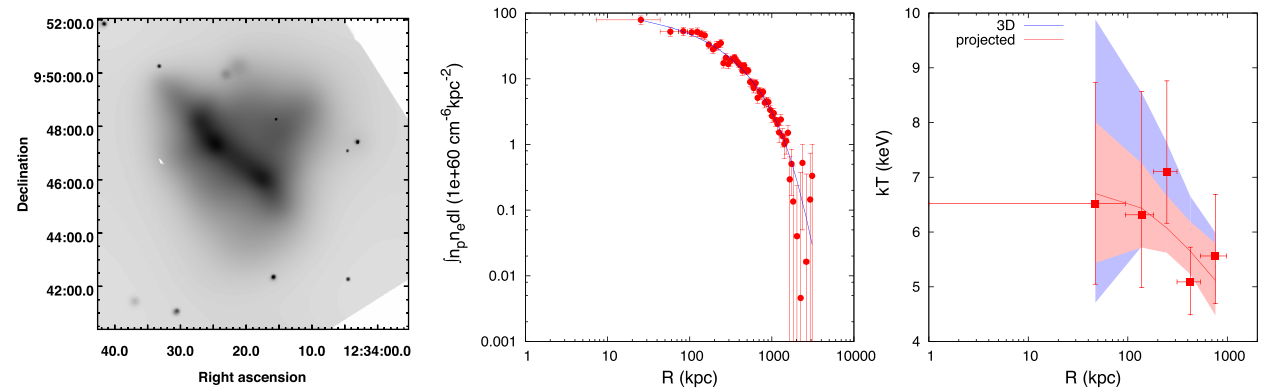

Figure C14. Same as Fig. C1 but for Z5247.

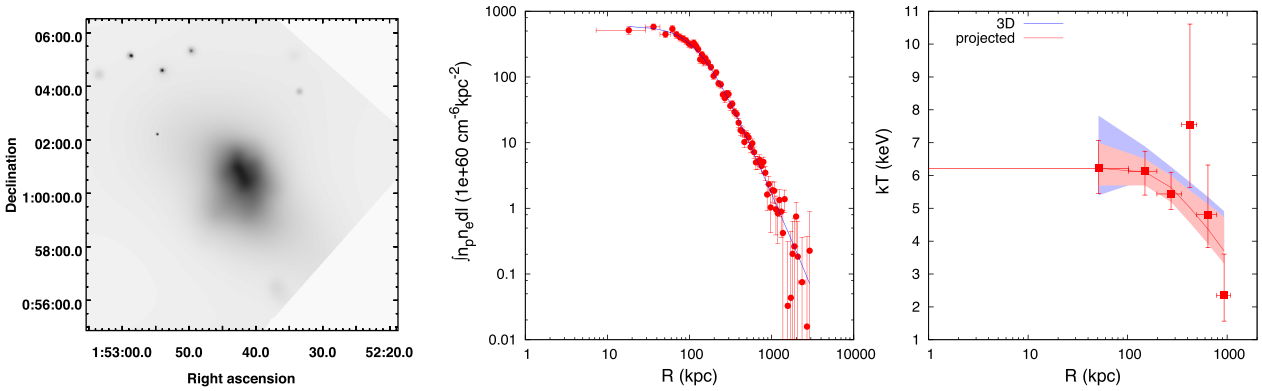

Figure C15. Same as Fig. C1 but for A267.

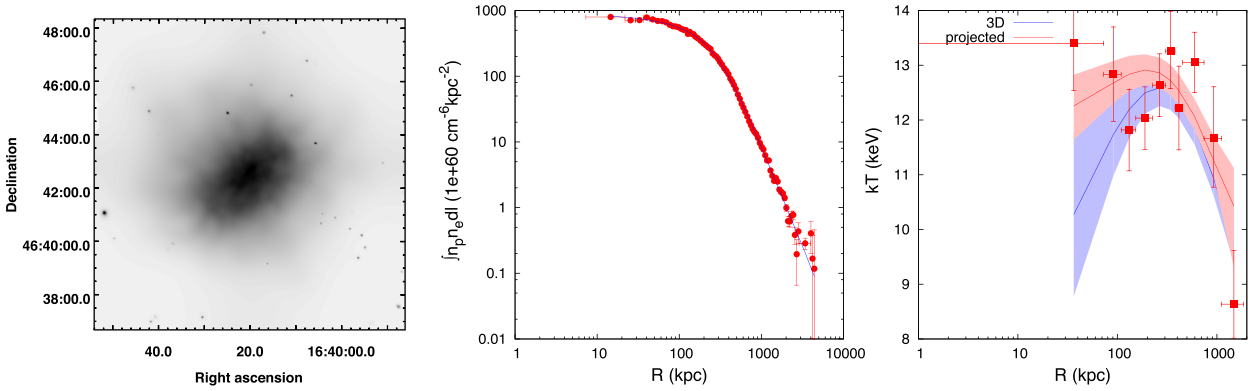

Figure C16. Same as Fig. C1 but for A2219.

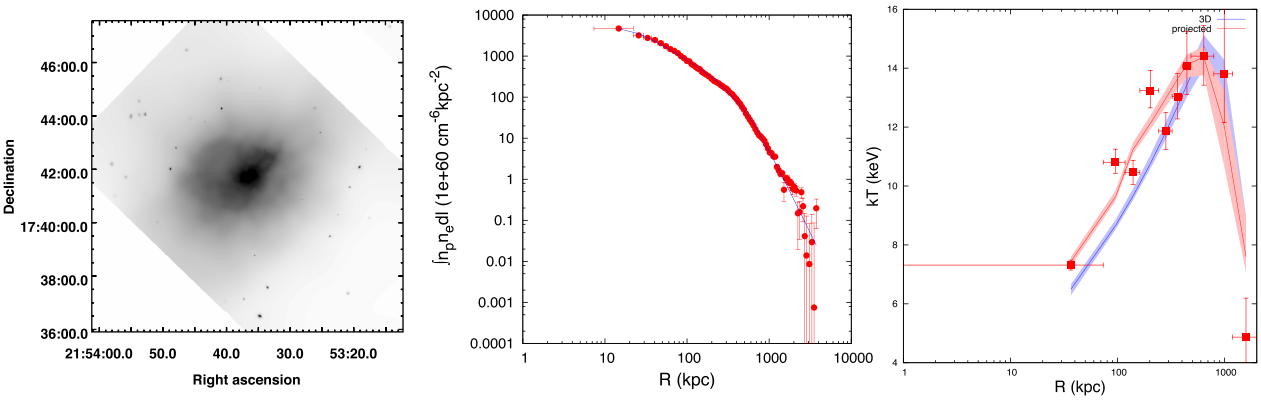

Figure C17. Same as Fig. C1 but for A2390.

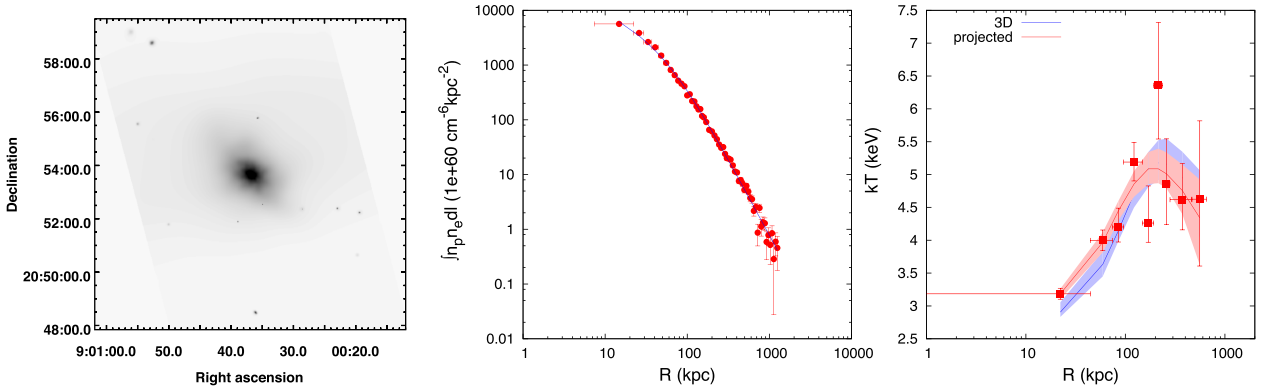

Figure C18. Same as Fig. C1 but for Z2089.

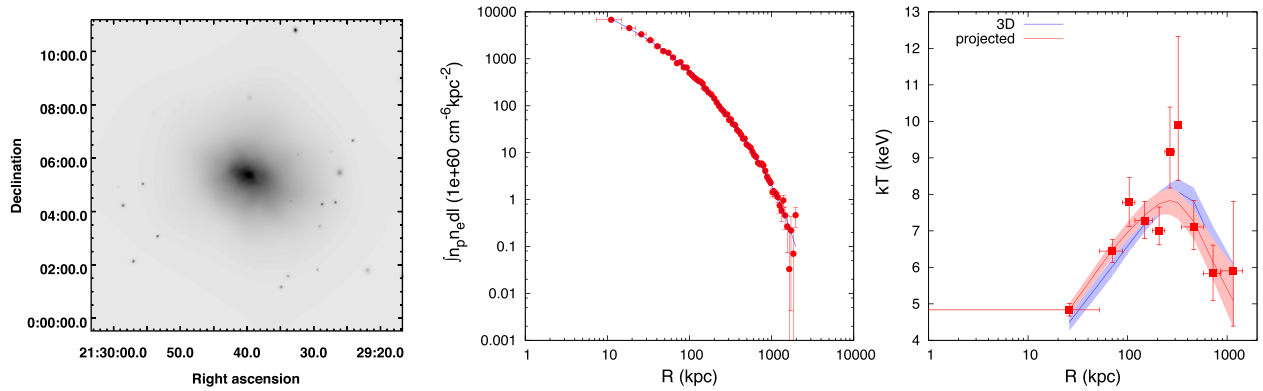

Figure C19. Same as Fig. C1 but for RXJ2129.6+0005.

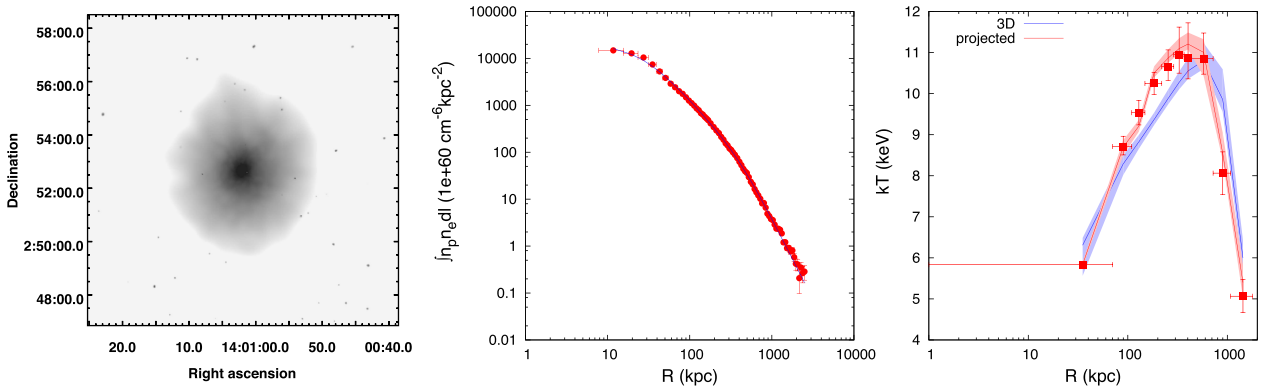

Figure C20. Same as Fig. C1 but for A1835.

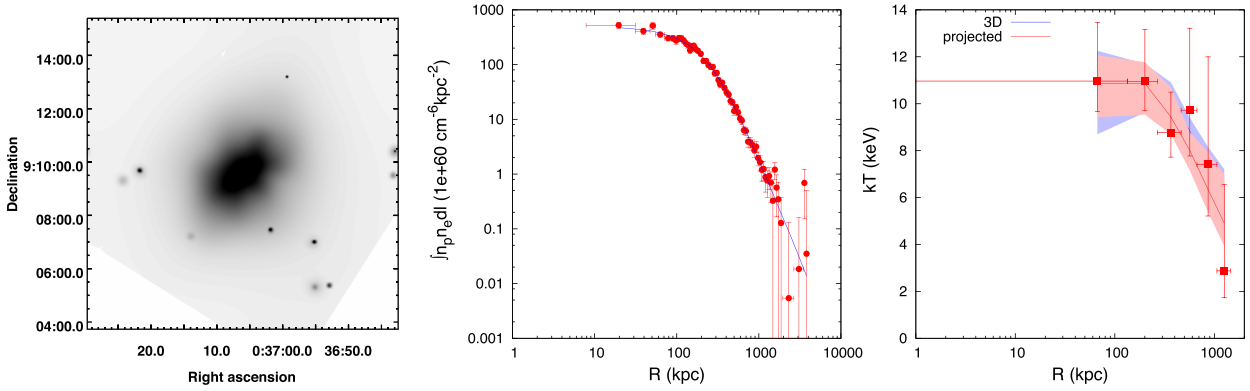

Figure C21. Same as Fig. C1 but for A68.

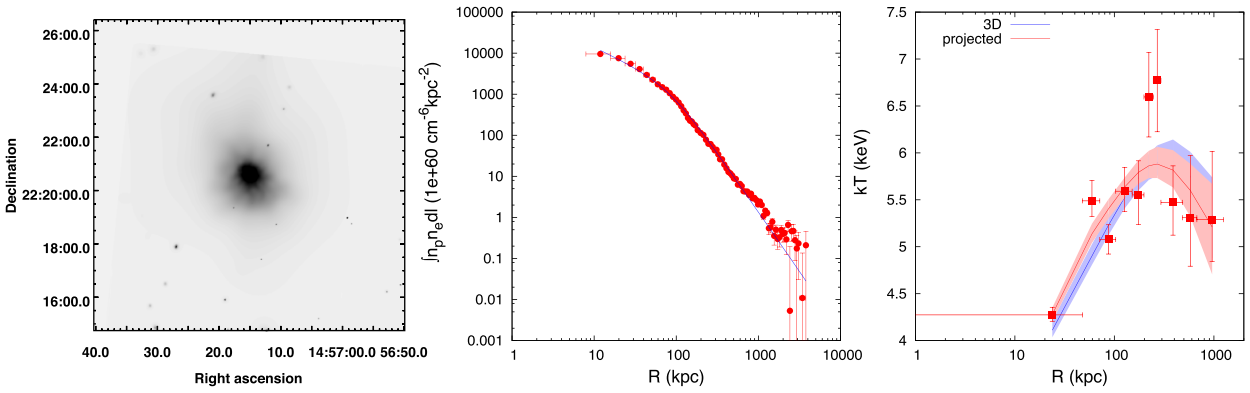

Figure C22. Same as Fig. C1 but for MS1455.0+2232.

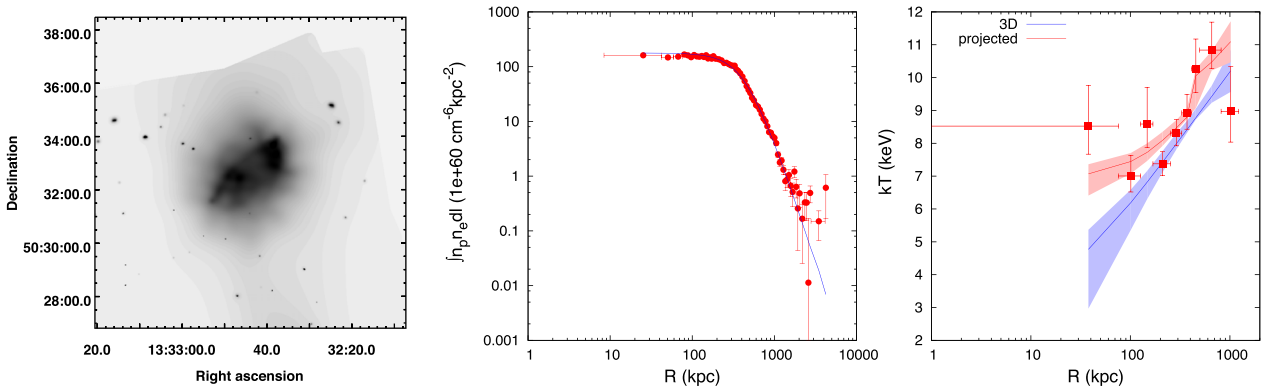

Figure C23. Same as Fig. C1 but for A1758.

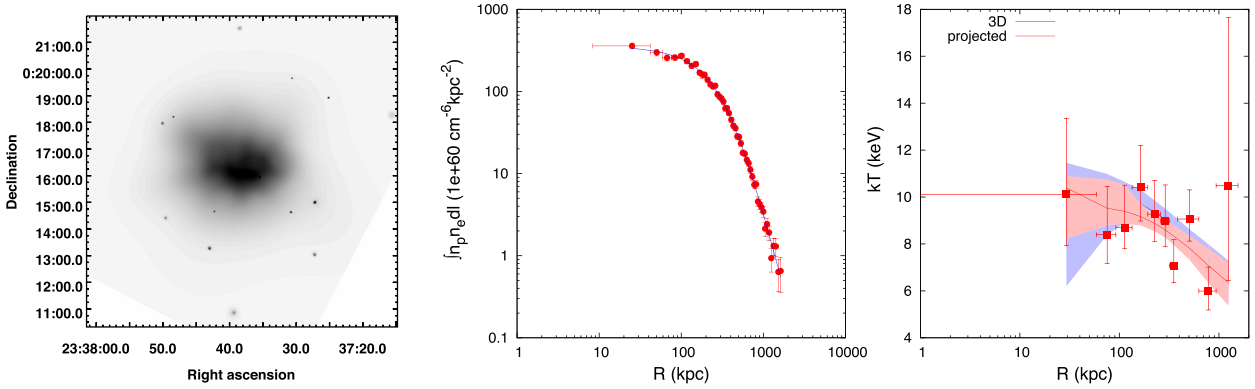

Figure C24. Same as Fig. C1 but for A2631.

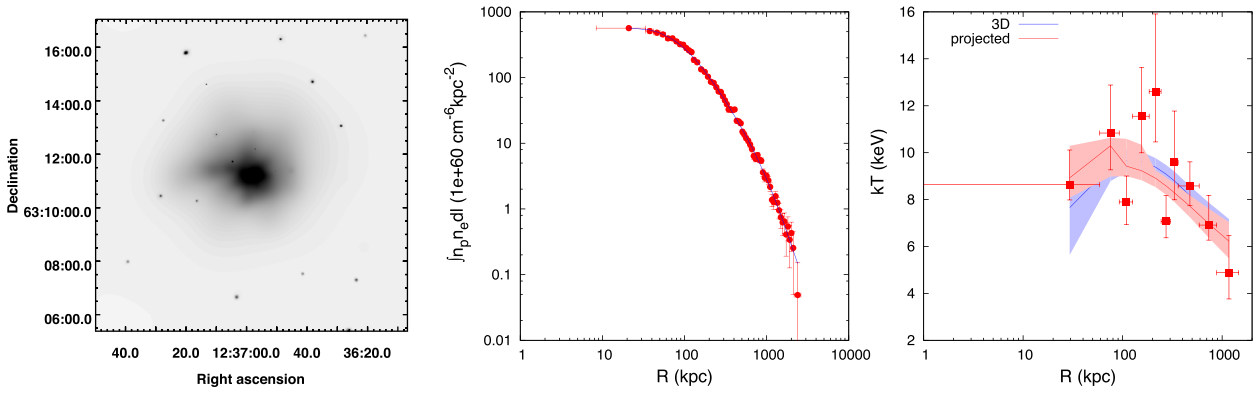

Figure C25. Same as Fig. C1 but for A1576.

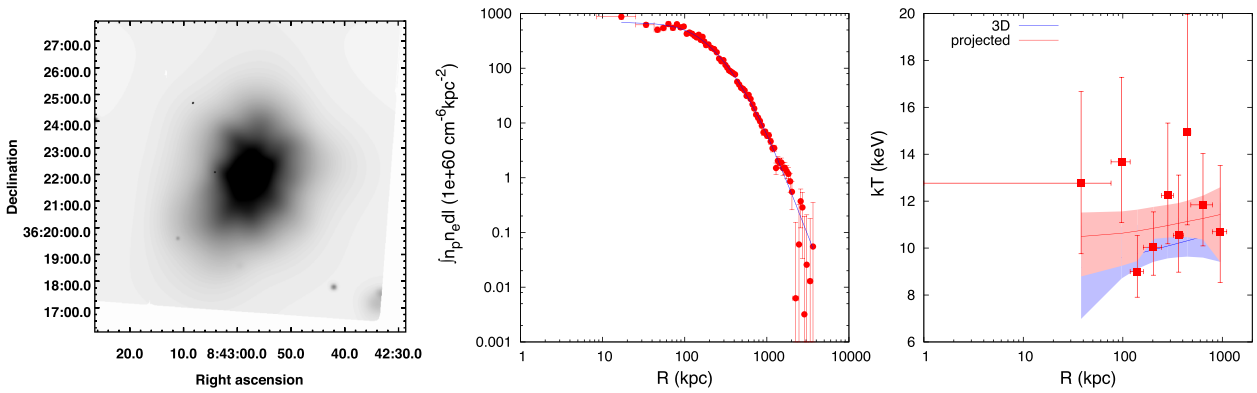

Figure C26. Same as Fig. C1 but for A697.

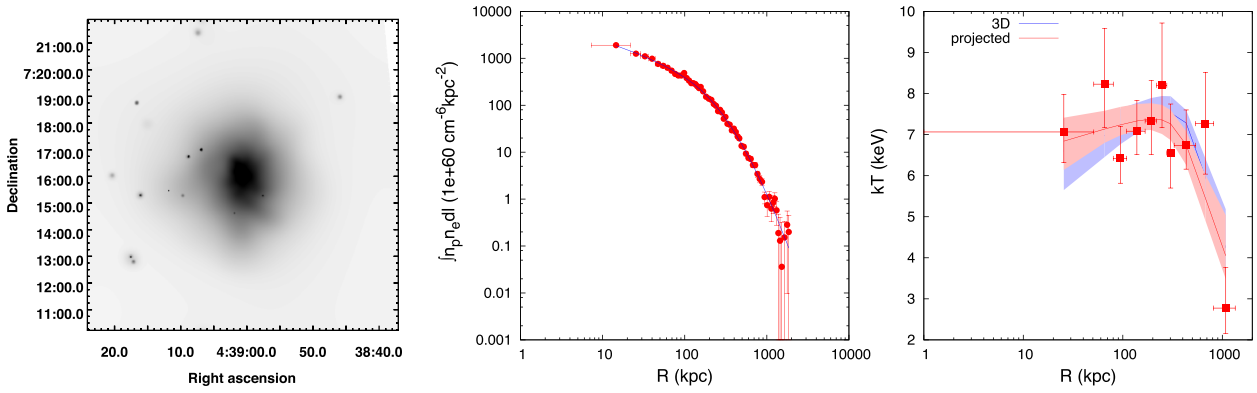

Figure C27. Same as Fig. C1 but for RXJ0439.0+0715.

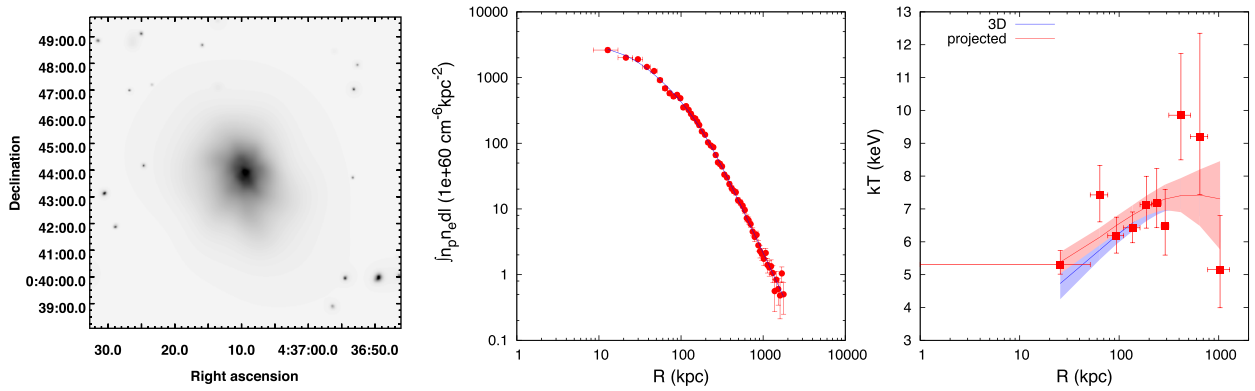

Figure C28. Same as Fig. C1 but for RXJ0437.1+0043.

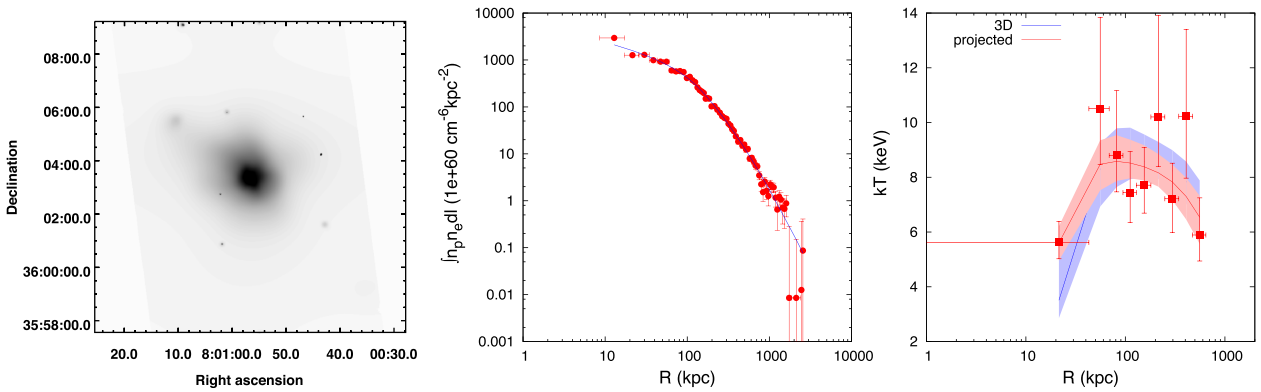

Figure C29. Same as Fig. C1 but for A611.

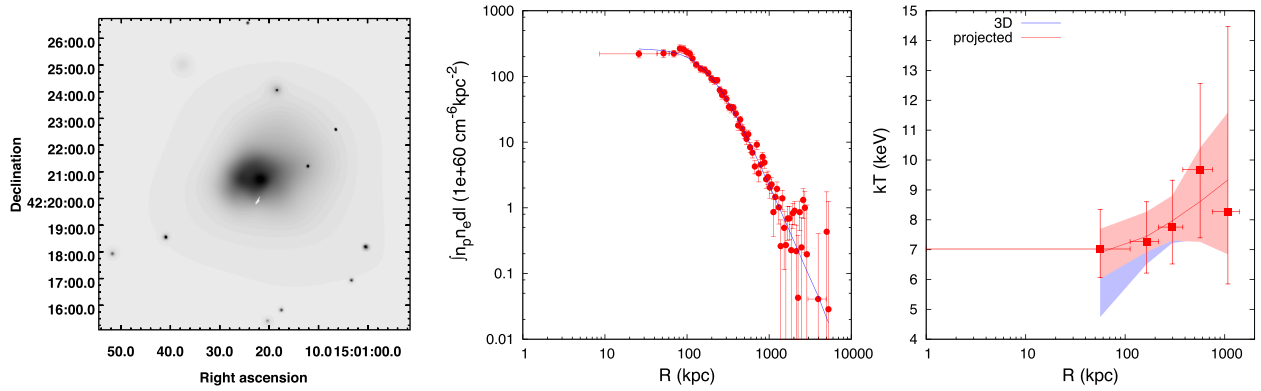

Figure C30. Same as Fig. C1 but for Z7215.

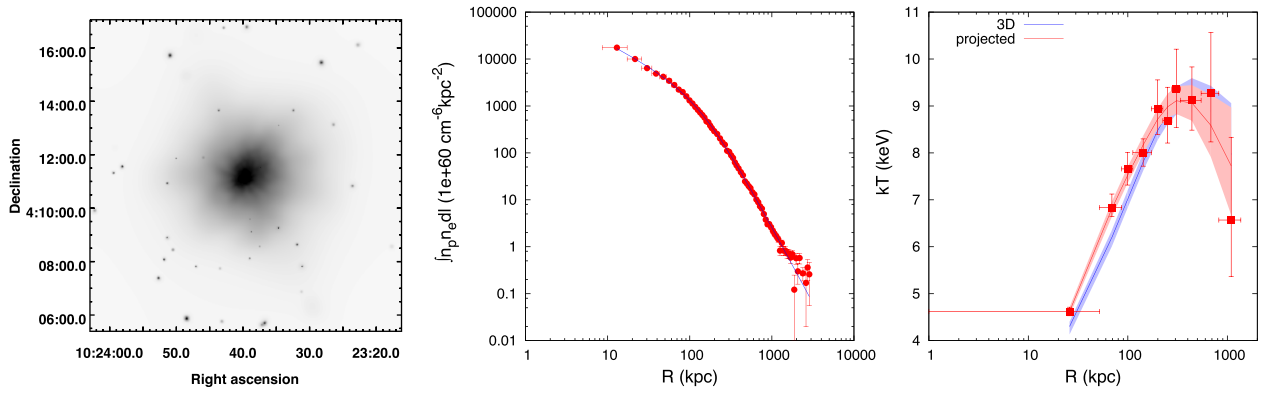

Figure C31. Same as Fig. C1 but for Z3146.

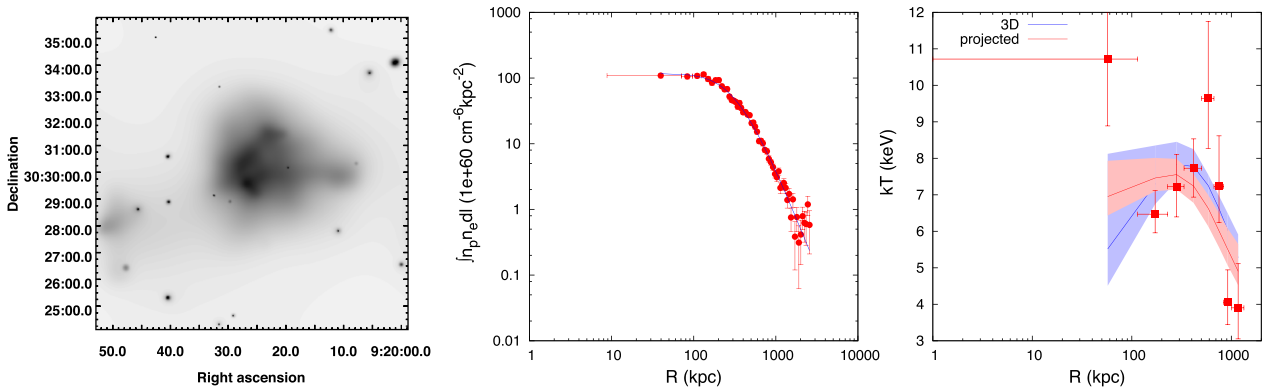

Figure C32. Same as Fig. C1 but for A781.

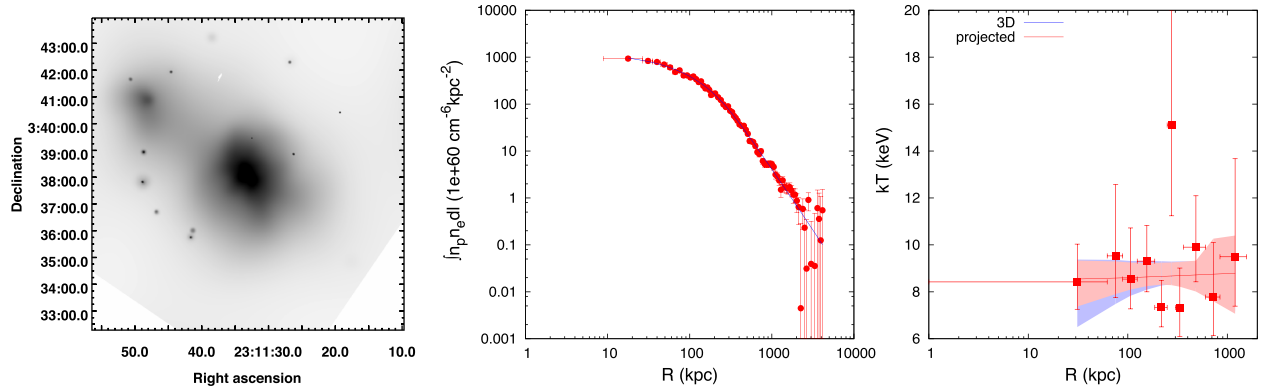

Figure C33. Same as Fig. C1 but for A2552.

This paper has been typeset from a TEX/LATEX file prepared by the author.